Journal of Structural Geology 146 (2021) 104304

Contents lists available at ScienceDirect

Journal of Structural Geology

journal homepage: http://www.elsevier.com/locate/jsg

Fault-induced mechanical anisotropy and its effects on fracture patterns in crystalline rocks

Pietari Skyttä [a,*], Nikolas Ovaskainen [a,b], Nicklas Nordbäck [b], Jon Engström [b], Jussi Mattila [a,c]

[a] University of Turku, Department of Geography and Geology, University of Turku, FI-20014, Finland
[b] Geological Survey of Finland, P.O. Box 96, FI-02151, Espoo, Finland
[c] Rock Mechanics Consulting Finland, Vantaankoskentie 14, FI-01670, Vantaa, Finland

ARTICLE INFO

Keywords:
Fault
Strike-slip
Damage zone
Mechanical anisotropy
Fracture domain

ABSTRACT

We used drone-acquired orthophotographs to map the 2D-networks of fractures transecting the Mesoproterozoic Rapakivi granites in southern Finland. The work aims at understanding i) how discrete faults and the kinematically linked syn-fault extension fractures originate in crystalline rocks, and ii) how the resulting structural anisotropy controls the patterns of later-formed regional fractures. We recognized incipient faults with associated distinct damage zones (DZ; wall-, tip-, bend- and linking damage) indicating that faulting occurred within mesoscopically isotropic material devoid of pre-existing fabrics. Moreover, fault-induced extension fractures occur also outside the normal DZs indicating much wider DZs than that predicted by scaling laws. Extension fractures within the wide DZs are the result of linkage between sub-parallel segments of the dominantly sinistral and ~N-S trending (sub-) vertical faults. The resulting syn-fault network of N-S, NW-SE and NE-SW trending fracture sets contributed to the mechanical anisotropy that controlled the patterns of the later-formed regional fractures. Specifically, i) narrow fault reactivation damage zones caused deviations in the patterns of otherwise systematic near-orthogonal regional fractures, and ii) the NNW-SSE trending regional fractures are poorly developed in areas where either several N-S faults or sub-parallel NW-SE syn-fault extension fractures are dominant. The latter applies in particular to a large left step-over zone between sinistral faults, which we infer to provide the first-order control over the development of contrasting fracture domains. The results of this study further indicate that a strike-slip paleostress event affected the crust after ca. 1.65 Ga.

1. Introduction

Understanding the systematics of fracturing within a crystalline bedrock is of primary importance in engineering geology, groundwater management, hydrocarbon exploration and nuclear waste disposal (Laubach et al., 2019). The relationship between in-situ stresses and rock fracturing is generally well-known from both theoretical (Pollard and Segall, 1987) and empirical rock mechanical studies (Kranz, 1983), which have shown how variable stress states (magnitude and orientation) and rock properties (including anisotropy) affect the orientation and type of fractures formed (e.g. Amadei, 1996; Pollard and Aydin, 1990; Segall and Pollard, 1980). Applying the principles of rock mechanical behavior to studies of bedrock fracturing introduces an overriding problem as the (paleo) stress responsible for the generation of the observed fractures has to be indirectly inferred from the structures and kinematic indicators. Investigations linking paleostresses to the fracture pattern are challenged by complexities within fracture patterns caused by i) polyphase deformation leading to several fracture generations and challenges in reliable determination of the relative ages of the fractures (Peacock, 2001; Scheiber and Viola, 2018), ii) structural inheritance (Mancktelow and Pennacchioni, 2005; Samsu et al., 2020; Skyttä and Torvela, 2018), iii) reactivation (Dutta and Mukherjee, 2019; Mattila and Viola, 2014; Rawnsley et al., 1992; Viola et al., 2009), iv) compositional heterogeneities, such as the grain size of the (intrusive) rocks (McCaffrey et al., 2003) and layering within sedimentary rocks (Carlini et al., 2019; Douma et al., 2019; Procter and Sanderson, 2018), and v) the structural anisotropy of the bedrock.

Considering the control of pre-existing structural heterogeneity on fracture generation, microscopic-scale heterogeneities are inferred to act as nucleating sites for micro-fractures (Anders et al., 2014; Crider, 2015; Griffith, 1921), whereas mesoscopic to macroscopic planar structures such as bedding, foliation or shear planes exert a strong

* Corresponding author.
E-mail address: Pietari.Skytta@utu.fi (P. Skyttä).

https://doi.org/10.1016/j.jsg.2021.104304
Received 1 October 2020; Received in revised form 4 February 2021; Accepted 9 February 2021
Available online 7 March 2021

control over the orientation of the generated fractures (Amadei, 1996; Behrestagni et al., 2018; Bose et al., 2020; Manda et al., 2008; Nejati et al., 2020). Furthermore, the relationship between brittle faulting and development of the damage zones (DZ) with pronounced fracturing are widely studied from the perspectives of fracture orientations (Woodcock and Fischer, 1986), types of damage zones (Kim et al., 2004; Peacock et al., 2017), delineation of damage zone extents (Choi et al., 2016), and damage zone extents as a function of slip magnitude or fault length (Faulkner et al., 2011; Perrin et al., 2016; Scholz, 2019). Whereas correlations between macroscopic deformation structures and fracture patterns exist for e.g. cylindrical folds (Bazalgette et al., 2010; Price, 1966; Stearns, 1969; Watkins et al., 2018) and previous works have also discussed structural inheritance at various scales – from faults to entire rift basins (Phillips et al., 2019; Rotevatn et al., 2018), the role of structural inheritance from tectonic faults on later-forming regional fracture systems has not been studied in detail yet. Evidence for structural inheritance from spatially extensive fractures on later-developed fracture networks does exist, but in such cases the early-formed fractures are typically related to non-tectonic features such as early diagenesis of platform carbonates (La Bruna et al., 2020; Lavenu and Lamarche, 2018) and thermal processes such as cooling of intrusions (Crider, 2015; English, 2012; Petford, 2003; Pollard and Aydin, 1990; Sanders et al., 2003; Segall and Pollard, 1983; Yuguchi et al., 2012).

In this paper we show that the formation of discrete faults and kinematically associated syn-fault extension fractures in mesoscopically isotropic rocks resulted in a mechanical anisotropy into the bedrock, which further controlled the patterns of the later-formed fractures ("regional fractures" hereafter). We further infer that such structural control is responsible for generation of specific fracture domains in which the present-day fracture patterns selectively reflect both the syn-fault evolution and the later-formed fractures. We also show that sub-parallel segments of incipient faults may be linked by syn-fault extension fractures, resulting in much wider damage zones than that predicted by existing scaling laws.

We conduct the investigation on the islands of Orrengrund and Båksören, Gulf of Finland, which provide a good coverage of high-quality glacially polished outcrops for 2D mapping of fracture and fault traces in anorogenic 1.6 Ga Rapakivi granite (Fig. 1). The bedrock of this area is homogeneous and mesoscopically isotropic, and transected by discrete faults which are associated with syn-fault extension fractures, both later overprinted by regional fractures of an unspecified origin. Moreover, the slip magnitude of the faults is limited (<20 cm), which provides an exceptional view into the early evolution of faulting and DZ generation. These prerequisites allow us to investigate the faults and related structures, and evaluate their effect upon the development of later fractures, without the need to account for further mesoscopic crustal anisotropy (e.g. foliation), complex deformation histories and (other) pre-existing structures.

We approach the research problems through fracture and fault mapping from drone-images supplemented with reconnaissance field observations (Table 1). Assigning the relative timing of the different fracture types (using fracture terminology according to Peacock et al., 2016) is an essential element of this work, and we base our interpretation on the abutting/cross-cutting relationships (see e.g. Peacock, 2001) and fracture patterns observed in the field and from the drone-acquired images. We characterize the discrete faults (kinematics and damage zones) and use the results in distinguishing the syn-fault extension fractures from the subsequent regional fractures. Thereafter, we develop our findings into a spatial fracture model of the site, including insight into i) the paleostress constraints, ii) strain localization patterns, and iii) how this understanding may be used in sub-dividing the area of interest into fracture domains characterized by contrasting fracture properties. We further discuss the plausibility of the fracture domain subdivision in the light of fracture connectivity analysis (relative proportion of X-, Y- and I topological nodes; Manzocchi, 2002) and orientation distribution within the delineated fracture domains.

This work contributes towards understanding the coupled evolution of the discrete faults and bedrock fracturing. The results add up to the so far incomplete database of brittle deformation events of the bedrock of Fennoscandia (Mattila and Viola, 2014; Viola et al., 2011). This investigation further provides an excellent dataset for future investigations focusing in the rock mechanical behavior of faults and their effect on fracture distribution in a crystalline bedrock.

2. Geologic setting

The bedrock of the study area is part of the anorogenic Mesoproterozoic 1.65–1.62 Ga Wiborg batholith (Rämö and Haapala, 2005) which was emplaced under an E-W extensional regime (Haapala and Rämö, 1992; Korja and Heikkinen, 1995; Nironen, 1997) associated with upward bulging of the mantle (Haapala and Rämö, 1992; Luosto et al., 1990) and emplacement of NW-trending diabase dykes (Rämö and Haapala, 2005). The batholith emplacement was potentially controlled by reactivation of subduction-related weak zones within the lithospheric mantle (Haapala and Rämö, 1992; Rämö and Haapala, 2005) or listric shear zones that caused extension within a thickened crust (Korja and Heikkinen, 1995). However, there are no studies known to the authors with evidence of localized deformation or penetrative tectonic fabrics within the rocks exposed at the surface. No significant compositional variation or separate intrusive units are present within the study area

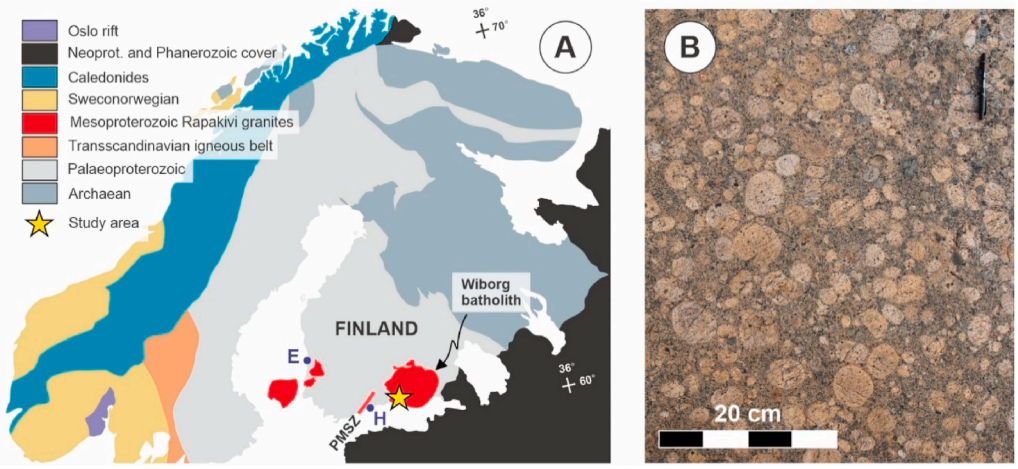

Fig. 1. A: Geological setting of the study area. E = Eurajoki, H= Helsinki, PMSZ = Porkkala-Mäntsälä Shear Zone (Pajunen, 2008). B: The mesoscopically isotropic character of the undeformed anorogenic Wiborg Rapakivi granite.

Table 1
Methods used and data used within this investigation.

ID	Task	Method/data	Results	Further used for	Notes
I	Orthophotography	Drone imaging	Orthophotographs of outcrops	III, VIII	Resolution of 0.55 cm/pixel
II	Field observations		Dip measurements, field notes	V, VI, VIII	From key areas
III	Fracture trace extraction	Manual digitization	2D fracture map of all fractures and faults	III-XI	37 075 traces from 73 200 m^2 area
IV	Fracture orientation analysis	Stereographic projections, visual inspection of trace maps, rose-plots[a]	Orientation-based sets	VI, VII, VIII	Length-weighted equal-area rose plots of all fracture traces[a]
V	Fault recognition and characterization	Visual inspection of trace maps; dip data	Fault traces, dips, kinematics and slip vectors	VII, VIII	Slip vectors determined mainly from the geometric relationship of the slip surface and DZ fractures
VI	Determination of fracture relationships	Visual and statistical inspection of abutting/cutting	Constraints over the relative ages of fractures	VII, VIII	Node data required for statistical inspection of fracture cross-cutting and abutting acquired using NetworkGT
VII	Determination of fracture relationships	Fracture set length distribution analysis	Power law modelled exponents for each fracture set	VIII	Fracture traces <1.8 m were cut from the fracture data to fit power law trend
VIII	Structural synthesis	Utilization of all prior analyses and interpretation	Structural interpretation of fault-evolution within the study area	X	
IX	Map variations in fracture intensity	Grid cell analysis of P21[b]	Contour map of P21	X	Circular sampling area, radius = 1.5 × 2m (contour cell width)[b]
X	Delineation of fracture domains	Structural interpretation and P21 contour map	Fracture domains	XI	

[a] Specification of rose-plots in Sanderson and Peacock (2020).
[b] P21 = Intensity per unit area; sampling strategy description in Fig. 3F by Nyberg et al. (2018).

Table 2
Summary of the recognized main faults and their characteristics.

	MAIN SLIP SURFACE			DAMAGE ZONE (DZ)			
	ID	Length (m)	Orient. (dipdir/dip)	Type of associated DZ (Peacock et al., 2017)	Fracture orientation (dipdir/dip)	Calc. shear direction[c]	Note
Sinistral	S1	180	079/83	Tip, wall, linking, bend	023/75	167/13	The main fault of the area
	S2	>25[a]	trend 342	Tip, interacting	trend 308	n.a.	
	S3	>48[b]	084/88	Wall, linking	026/69	173/23	Observed slip lineation 158/10
	S4	>31[a]	076/74	Tip	024/69	162/4	
	S5	>39[a]	trend 346	Tip	trend 295-314	n.a.	
	S6	>21[b]	trend 347	Tip	n.a.	n.a.	Stepped DZ fractures, no distinct trend
	S7	>12[b]	276/86	Wall	037/61	189/34	
	S8	>21[b]	trend 347	Wall	trend 305	n.a.	Fault inferred from secondary fractures
Dextral	D1	>65[b]	102/84	Tip, linkage, wall	161/74	014/15	5 cm slip along secondary slip surface
	D2	>20[b]	086/88	Linkage, tip	149/76	357/14	Potential continuation of D1
	D3	>115[a]	trend 293	Interaction, linkage	trend 355	n.a.	Linked to S1 & S2
	D4	>35[a]	133/86	Tip, wall	178/80	044/09	
	U1	>27[a]	trend 358	Tip	n.a.	n.a.	Two parallel zones; conflicting kinematics

[a] Length open from one end.
[b] Length open from both ends.
[c] Based on the geometrical relationship between the main slip surface and the DZ fractures: the slip vector is perpendicular to the line of intersection of the main slip surface and the DZ fractures (Fossen, 2016).

(Fig. 1) and any potential structural anisotropies correspond to weak magmatic foliations (Karell et al., 2014) or the presence of quartz-feldspar porphyry and diabase dykes, and greisen or quartz veins (Rämö and Haapala, 2005). Particularly interesting for the Loviisa area are the two sets of Indium-rich polymetallic greisen veins: a set of NE to NNE trending veins and the slightly younger set of NW-NNW trending veins (Generations 2a and 2b by Broman et al., 2018; Valkama et al., 2016). Regionally occurring barren opening-mode fractures transecting the intrusion comprise two subvertical NE-ENE and NW-NNW striking sets (Ovaskainen, 2020) and one sub-horizontal set, defining an overall cubic fracture pattern in 3D (Okko et al., 2003).

3. Methods

The relevant methods, data and workflow are outlined in Table 1. The core of data used within this investigation is formed by aerial photographs acquired by UAV at a flight elevation of 20 m, resulting in a pixel size of 0.55 cm for the output raster images. We took the drone images with a minimum of 60–70% overlap, georeferenced the images using 10 VRS-GPS ground control points for each surveyed area and processed the aerial photos into orthomosaics with Agisoft PhotoScan software (v1.4.4., 2018). 2D-map of fault and fracture traces exposed on the glacially polished outcrops of the Orrengrund and Båksoren islands are compiled using the orthophotographs and subsequently supplemented with reconnaissance field observations of fracture characteristics and dips. The dataset includes 37 075 fracture and fault trace lines manually digitized in ArcGIS software from an area of 73 200 m^2 (Appendix 1). The well-exposed outcrop parts typically extend 50–100 m inland from the coast line along the southern and western shores of the Orrengrund and Båksören islands, whereas the exposures in the North

and East are narrow and discontinuous (Fig. 2; Appendix 2).

As the first step of our structural analysis, we analyze the orientation of all the trace lines with length-weighted equal-area rose plots (Sanderson and Peacock, 2020) and visual inspection of fracture trace maps (Table 1). Visual inspection is required because a purely rose plot -based orientation analysis would fail to capture fracture sets that contain the N-S-striking faults and syn-fault fractures due to their relative scarcity and spatial variance compared to the more through going nature of the regional fractures. Subsequently, we use the generated fracture trace dataset and field observations to recognize discrete faults (Fig. 3a and b), for which we define the damage zones (DZ; Peacock et al., 2017); by visually delineating the extent of mutually (sub)parallel fractures, which are spatially associated with the N-S faults and deviate from the trends of the regional fractures (see e.g. Fig. 4). We analyze the kinematics of the faults using the very limited amount of observed offsets markers and fault surface slip lineations. As very few lineation data are available due to the 2D-nature of the glacially polished outcrops, we use the geometrical relationships between the slip surfaces and the dominant set of kinematically associated syn-fault fractures within the damage zones to determine the shear direction – the slip vector is perpendicular to the line of intersection of the main slip surface and the DZ fractures (Fossen, 2016) – and to provide a first-pass assessment about the regional paleostress domain responsible for the faulting.

Subsequently, we utilize these results to distinguish between the fault-induced fractures and the regional fractures particularly outside the direct damage zones of the faults. To support the visual analysis, we analyze the fracture Set length distributions and topological relationships to reveal potential linkages to the faults and to support the field observations about the relative timing between the fracture Sets. We analyze the topological cross-cutting and abutting relationships using a spatial intersect analysis of fracture traces and nodes acquired with NetworkGT software (Nyberg et al., 2018). We use the proportion of Y- and X-nodes between selected Sets and abutment relations for each of the observed Y-nodes, plot the node counts for a selected pairs of fracture Sets on bar plots, and use qualitatively to interpret the relative timing of fracture Sets. This approach does not use the lengths of the traces that form the nodes as any kind of weights and we therefore limit this analysis to traces over 5 m in length to filter out the numerous smaller fractures. The method has its limitations as we do not quantify the statistical significance of the relative node count proportions depending on at least the number of traces in each set and the total node count sample size, and because the fracture Set classification is purely orientation-based.

We model Set length distributions using a power law trend (Bonnet

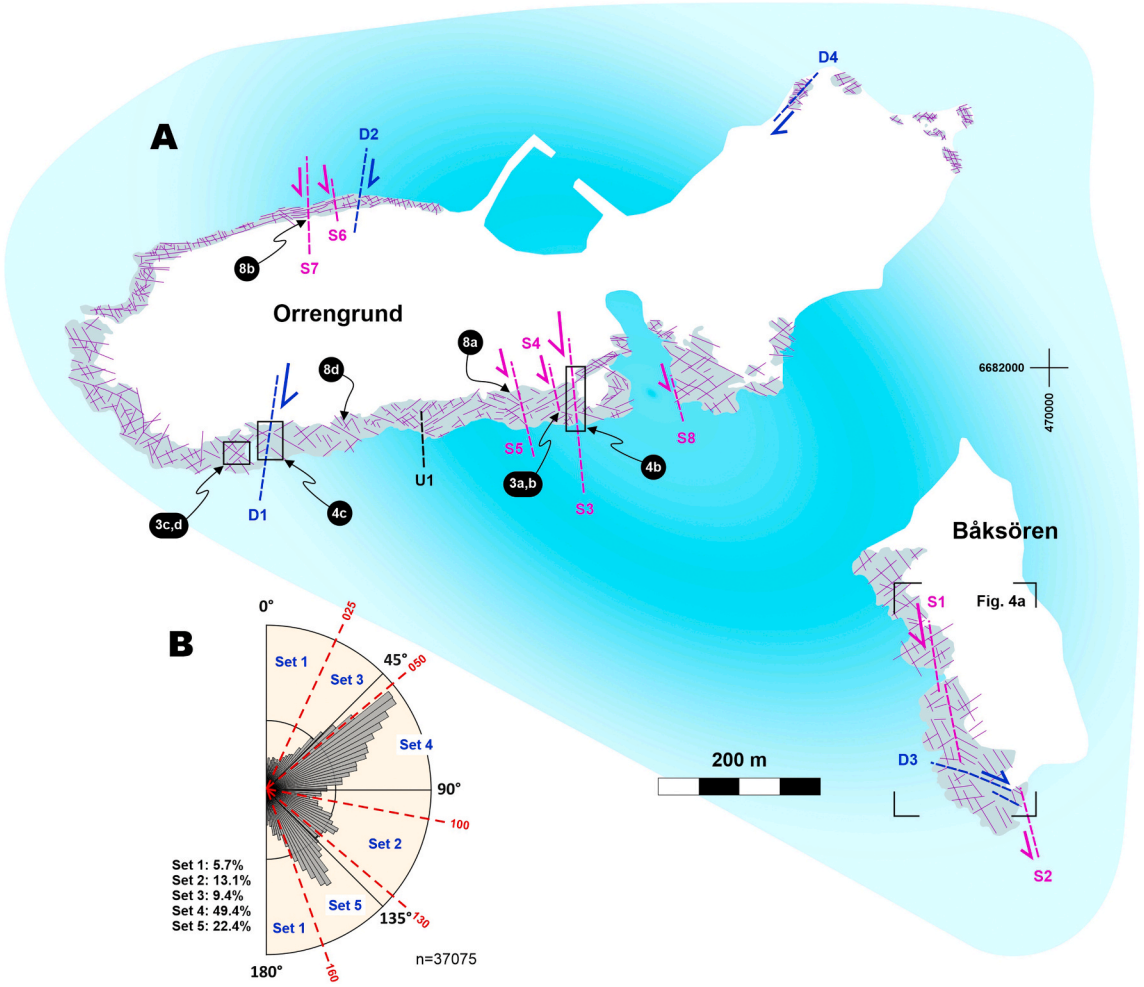

Fig. 2. A) An overview of the Orrengrund and Båksören islands showing the areas covered by UAV-mapping (grey), the dominant fracture trends (thin magenta lines) and the recognized first-order faults (dashed lines). The traces of faults with dextral, sinistral and unknown kinematics (Table 2) are shown with blue, magenta and black dashed lines and labelled with letters "D", "S" and "U", respectively. Lettering within the black circles refers to other figures. Coordinates are in EUREF_FIN_TM35FIN. B) An equal-area length-weighted rose diagram illustrating the orientation distribution of all the mapped discontinuities (fault and fracture traces) and their subdivision into orientation Sets for the purposes of further analysis (Section 4.3). The percentages indicate the share of traces included within one Set as calculated from the total length of all the traces. North is up in all the maps in this paper. (For interpretation of the references to color in this figure legend, the reader is referred to the Web version of this article.)

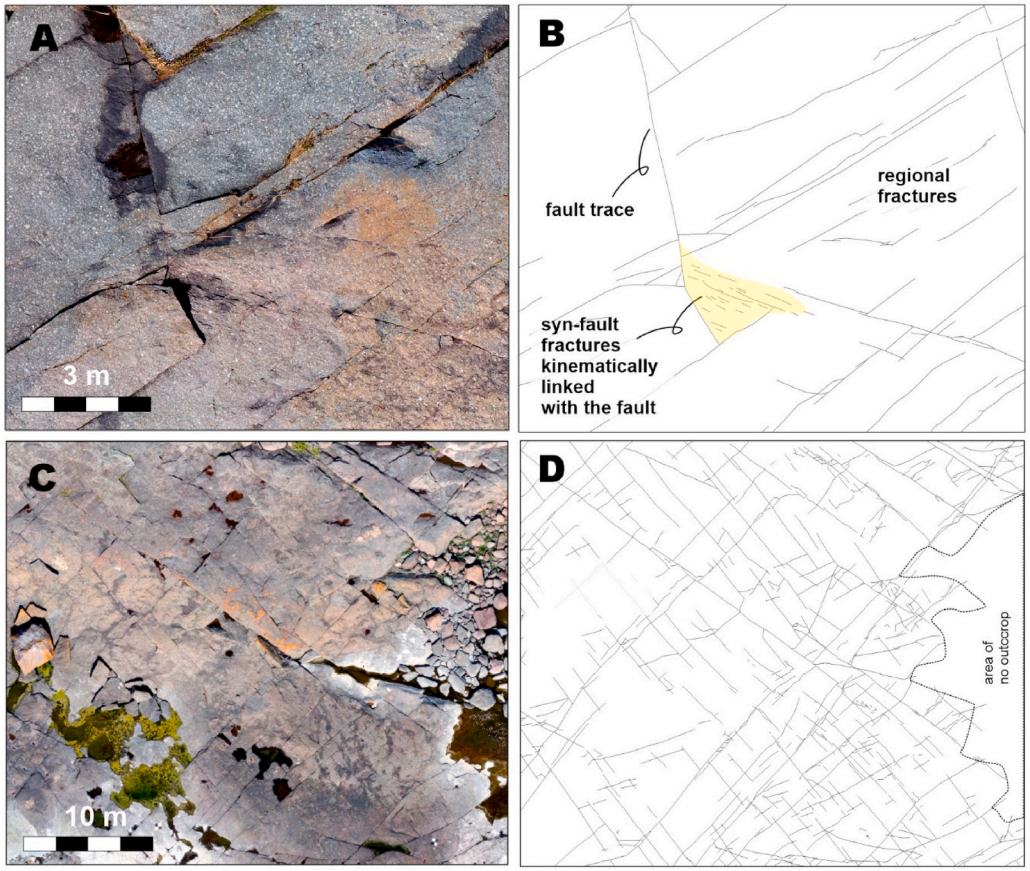

Fig. 3. Examples of the UAV images (A, C) and the resulted fracture trace interpretations (B, D). A and B: Clearly recognizable, kinematically linked wing-crack type extension fractures defining a tip-DZ at the Southern termination of the sinistral N-S striking vertical fault S4. C and D: A site outside the apparent influence zones of the discrete faults displaying four dominant orientation sets but less clear relative timing relationships among the fractures. See Fig. 2 for image locations.

et al., 2001) to assess the correlation between origins of the Sets (fault, syn-fault extension fracture or regional fracture) and the Set length distribution characteristics. According to Davy et al. (2010), fractures formed in low fracture density conditions grow freely without much interference from other fractures whereas fracture growth rate in high density conditions is limited by other fractures. Differences in growth rate are reflected in the exponent of the fitted power law model, with e.g., lower negative exponent correlating with growth conditions with high fracture density. The resolution of the orthophotographs sets a minimum limit to the length of fracture traces that are accurately digitized and consequently a portion of fractures starting from the smallest does not follow a power law trend. Therefore, a minimum trace length i.e. a cut-off is applied by cutting all fracture traces smaller than the visually determined cut-off (1.8 m) from the length distribution data and then fitting the power law trend to the remaining distribution data. This is a simple approach for modelling the length distributions with limitations, but a deeper analysis of the set-wise length distributions is outside the scope of this paper. Subsequently, we make a structural synthesis over the fault-evolution of the site, explaining the relationship between the faults and the syn-fault fractures. We use this synthesis along with fracture intensity (P21; Dershowitz and Herda, 1992); in evaluating how the resulted fault-induced structural anisotropy controlled subsequent fracturing and develop the findings into a preliminary fracture domain model explaining the contrasts in fracture patterns across the study area. Finally, we discuss the findings from the perspective of the evolution of brittle deformation in the Fennoscandian Shield.

4. Structural data and observations

4.1. Overview

The studied rapakivi granite comprises up to 5 cm diameter feldspar ovoids embedded within a finer-grained groundmass of primarily feldspar and quartz. The rocks display minute variation in color and composition within the study area, are mescopically isotropic, and lack any recognizable fabrics visible to the naked eye (Fig. 1b). Within the aerial images from the study area, no gouge-bearing fault cores are recognizable. For this reason, we distinguished faults from other fractures primarily using the spatial patterns of the discontinuities, with support from field observations. As a result, several approximately N-S trending faults are recognized from associated damage zones characterized by obliquely oriented fractures abutting against the fault traces (Fig. 2a; 3a,b). Fracture patterns outside the faults and their immediate damage zones are more complex (Fig. 3c and d) and understanding their systematics requires that we first define which fractures are synchronous with, and kinematically associated to the faults, and what is their relationship with the remaining fractures. According to our findings reported in Sections 4.2.-4.5., and the recommended use of terminology (Peacock et al., 2016), we call the approximately N-S fractures “faults” (Set 1 in Fig. 2b). Fractures which are synchronous with, and kinematically associated to the faults are called syn-fault “extension fractures” (Sets 2 and 3 in Fig. 2b) as they originated as opening-mode wing-crack type fractures at the tip-DZs of the N-S faults. Some of the extension fractures were reactivated as “shear fractures” (Section 5.1). The remaining fractures, not associated with the faults, are hereafter called “regional fractures” (Sets 4 & 5 in Fig. 2b).

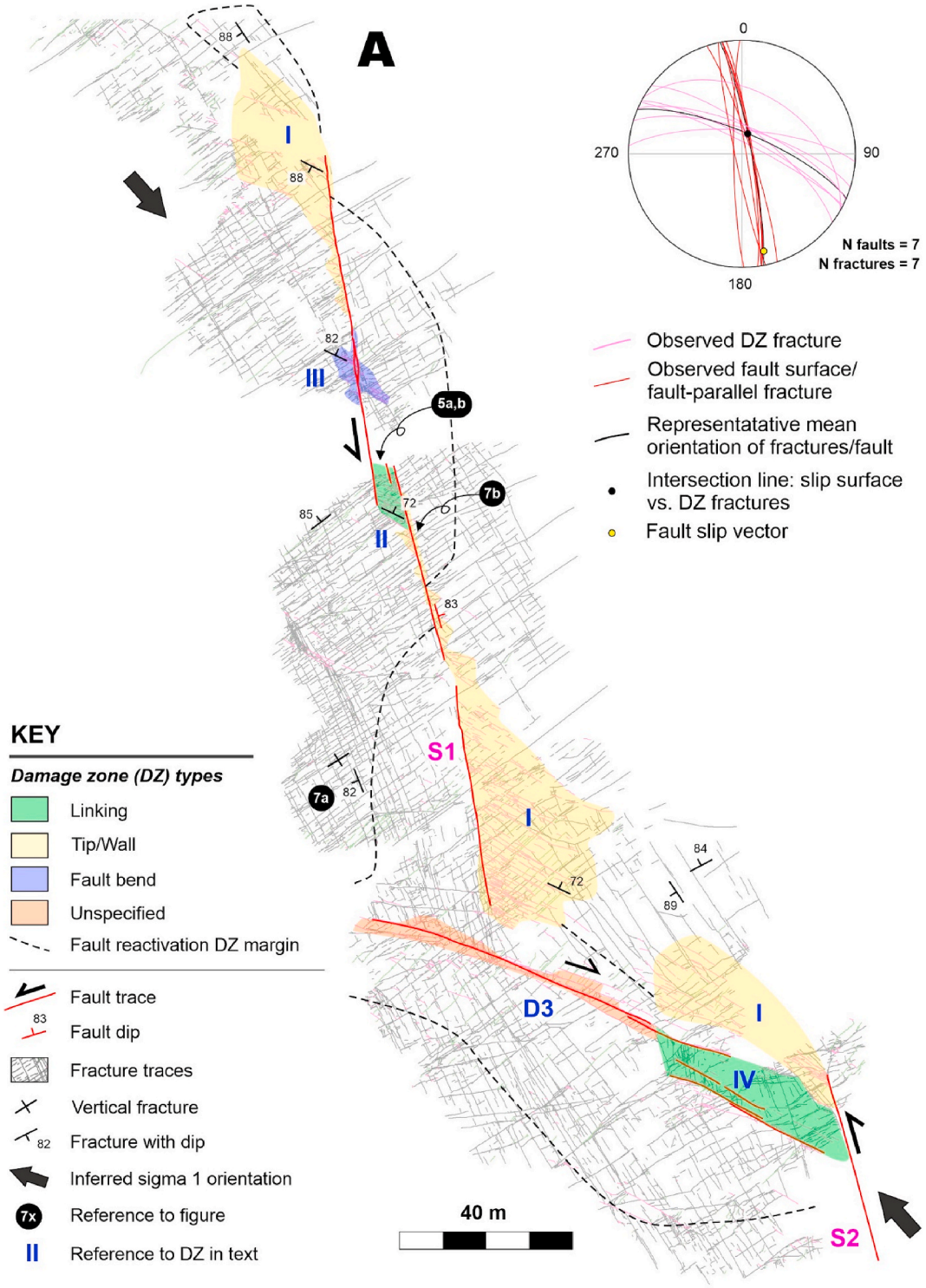

Fig. 4a. Maps of the recognized main faults and the associated syn-fault fractures within their damage zones. Fracture traces coloring: Sets 1, 4 and 5 = grey, Set 2 = purple, Set 3 = green. The lower hemisphere stereograms show the measured orientations of the slip surfaces and the dominant fractures and the derived slip vectors for the faults. A) Faults S1, S2 and D3. B) Fault S3. C) Fault D1. (For interpretation of the references to color in this figure legend, the reader is referred to the Web version of this article.)

4.2. Characterization of the N-S faults

Several discrete, approximately N-S trending sub-vertical faults, recognized from variably developed damage zones (Figs. 4, 5a and 6a; App. 2) and narrow gouge zones (Fig. 6b), cut the bedrock of the study area. We summarize the main properties of all the recognized faults in Table 2 and characterize the three most significant faults in more detail, with complementary field data.

Fault S1: S1 is the largest fault of the study area and it is exposed in full length on the Båksören Island (Figs. 2a and 4a). S1 dips steeply to the east, has a total lateral tip-to-tip extent of 180 m and is characterized by well-developed patterns of extension fractures within the damage zones (Figs. 4a and 5a,b; App. 1 & 2), all indicating sinistral sense of movement along the fault. The most distinctive DZs are of the combined wall/tip

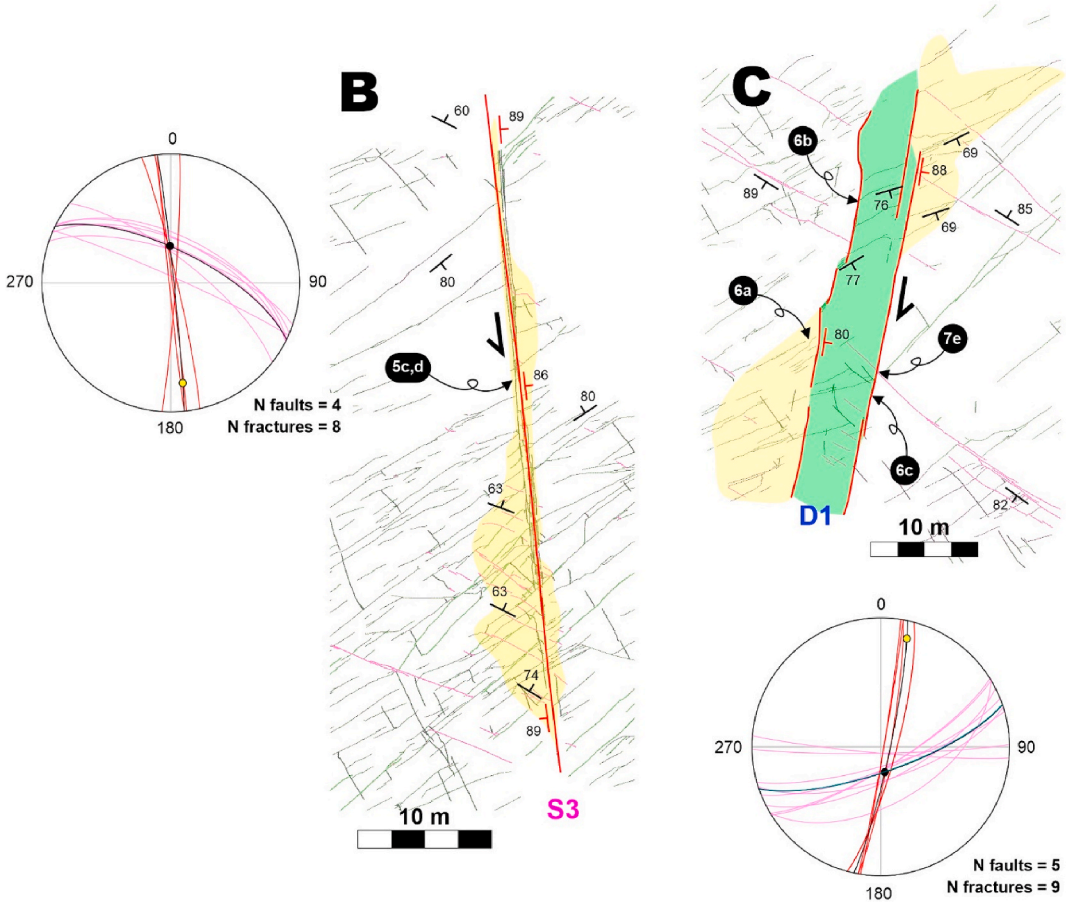

Fig. 4b. cont. Symbols as in Fig. 4a.

type, characterized by a pattern of wing-crack fractures oblique to, and abutting against the main fault close to its both terminations ("I" in Fig. 4a). The largest tip/wall DZ spatially associated with the southern fault termination is approximately 35m by 60m in width and length. The fault is comprised of two sub-parallel segments kinematically linked at the left-handed releasing step-over (linking DZ at "II"; Fig. 5a). The step-over hosts NNE-dipping fractures, some of which are locally infilled with quartz and pseudotachylyte. These dilatant veins indicate local extension of so-far undetermined magnitude (Fig. 5b). One further type of DZ is associated with a minor restraining fault bend, leading to the generation of short extension fractures defining a recognizable fault bend DZ on both sides of the fault ("III"). Fractures within all the DZs (with approximately 70° dips) are gentler than the regional fractures observed outside the DZs (80–90° dips). No slip lineation was observed in the field, but a sub-horizontal south-plunging (167/13; trend/plunge) slip vector indicative of strike-slip faulting could be determined from the relationship of the fault plane and the secondary fractures (Inset in Fig. 4a).

Continuous WNW-ESE trending extension fractures (Set 2) parallel with the wing-cracks at the southern tip-DZ constrain the southern extent of S1 and link it to another approximately N-S striking sinistral fault (S2). The linking WNW-ESE fractures are frequently arranged into a right-stepping pattern, and secondary fractures within the step-overs ("IV") indicates dextral sense of movement along these fractures. Consequently, the WNW-ESE features define the dextral fault D3.

Fault S3: The sub-vertical, N-S trending S3 fault has an observed trace length of 48 m but neither of the fault terminations are exposed (Fig. 4b): In the north, fracture patterns visible from the partially vegetated outcrops indicate fault continuity. To the south, the fault trace continues beyond the shoreline, and the fault is associated with a relatively wide wall-DZ. In the central part, the fault has a core domain defined by two slip surfaces separated by approximately 60 cm, and one of these exposes a sub-horizontally south-plunging slickenline lineation on a mica-rich fault surface (Fig. 5c). The volume between the slip surfaces contains a linking-type DZ characterized by fault-parallel minor faults, and fault-parallel and oblique fractures (Fig. 5d). Locally, linked systems of minor faults and extensional veins comparable to extensional pull-apart basins (Fig. 5d) have been developed. S3 is associated with a wall-type DZ which shows significant along-strike variations, reaching the largest extent (width 5 m, length 25 m) in the southern part of the fault. The DZ is defined by the presence of NNE-dipping extension fractures which dips are gentler with respect to the regional fractures. Fracture patterns within the linking and wall-DZ indicate sinistral sense of movement. Determination of the slip vector from the main fault and the secondary DZ-fractures results in a value of 173/23 which is comparable but slightly steeper than the observed slickenline lineation (158/10), both indicating dominantly strike-slip type deformation along the fault surface.

Fault D1: D1 is the largest recognized dextral fault of the study area with a minimum trace length of 65 m (the fault is unexposed from both terminations). D1 comprises of two sub-parallel, steeply east-dipping slip surfaces (Fig. 4c): the western, main slip surface is curved and shows two minor releasing bends, tip/wall-type DZ in the southern part (Fig. 6a), cataclastic deformation within the approximately 2 cm wide fault core (Fig. 6b), and local development of mm-wide pseudotachylyte veins along the slip surfaces. The eastern slip surface is more linear and characterized by a wall/tip DZ in the north, and several discrete small-scale extensional pull-apart basins generated along the strike of the surface, indicating approximately 4 cm slip offsets (Fig. 6c). Additional to the wall/tip DZs, linking DZ characterized by sparse, slightly curved

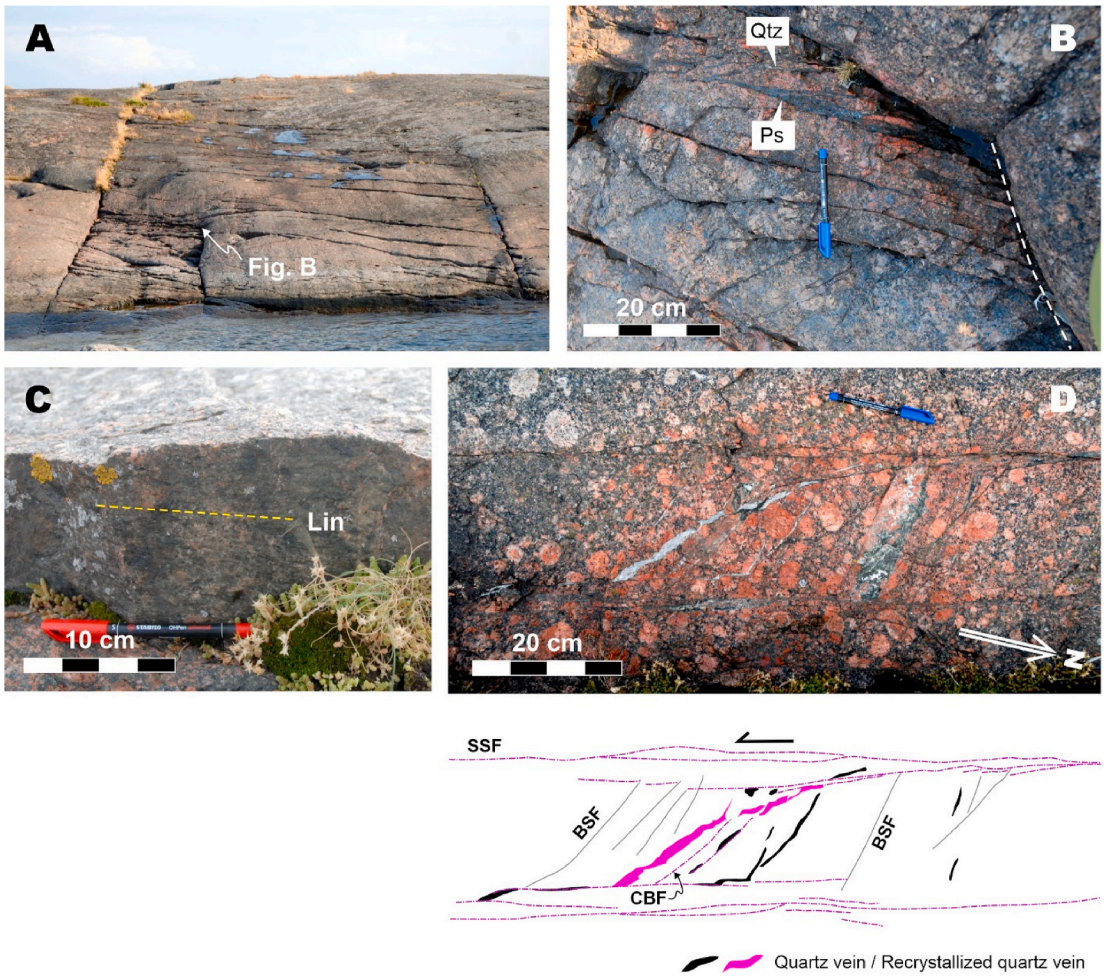

Fig. 5. Field characteristics of the sinistral faults and their damage zones. A) A major left-step formed by the N-S striking segments of the sinistral Båksören fault S1, with pronounced fracturing within the step-over damage zone. Distance between the overlapping fault segments is 5.5 m. View towards South. B) Quartz veins (Qtz) and pseudotachylyte melt (Ps) within the releasing step-over. View towards South. C) Sub-horizontal striation on the slip surface of the sinistral S3 fault, View towards East. D) Field photo and line drawing of the sinistral S3 fault comprising two parallel slip surfaces (SSF = standard strike-slip fault), joints and quartz veins delineating the margins of the developed pull-apart basin (comparable to the basin sidewall faults "BSF") and dynamically recrystallized quartz veins emplaced along the cross-basin faults (CBF; terminology after (Corti and Dooley, 2015; Dooley and McClay, 1997). *See* Figs. 2 and 4 *for the locations of the photos.*

NE-SW trending extension fractures has been developed between the slip surfaces. DZ fractures dip steeply to the SSE, with an average dips of 74°, which is clearly gentler with respect to the regional fractures (dips > 80°). The geometrical relationship between the fault surface and the secondary fractures (e.g. Fig. 6a) indicates sub-horizontal north-plunging slip orientation (014/15), compatible with a strike-slip faulting regime.

4.3. Relationships between fractures

4.3.1. Relative timing

Regional fractures belonging to the approximately orthogonally trending orientation Sets 1 and 2 (Fig. 2b) typically crosscut and abut each another (Fig. 7a), for which reason they may be considered synchronous. However, they either terminate against the N-S trending faults (Fig. 7b; fracture Set 1 in Fig. 2b), or their orientation or intensity locally changes in spatial vicinity with the faults (Section 4.3.). Consequently, based on abutting/cross-cutting relationship, we infer that, the regional fractures post-date the formation of the faults and syn-fault extension fractures (Section 4.2). Length and topology analysis of the fracture sets further supports the interpreted relative timing relationships: The continuous WNW-ESE trending fractures of Set 2 terminate at the N-S faults (Set 1; Fig. 7c and d), which, together with the demonstrated kinematic linkage (Fig. 4), indicates Set 2 generated synchronous with faulting. Sets 1 and 2 are further similarly characterized by longer, more continuous, traces indicated by the highest power law exponents of −1.55 and −1.52, respectively (Fig. 7c). By contrast, lower power law exponents (<-1.7) and abutment against Set 2 characterize the fracture Sets 4 and 5 (Fig. 7c and d), based on which fractures belonging to the dominant regional Sets 4 and 5 also post-date the faults and the syn-fault extension fractures of Sets 2 and 3.

Results of the topological analysis (Fig. 7d) conducted for data covering the whole study area do not clarify the relationship between the regional fractures and the NE-SW Set 3 fractures, kinematically linked to the N-S trending dextral faults D1 and D2. The reason is that the Set 3 fractures occur within a limited area spatially associated to faults D1 and D2, and are for this reason indistinguishable from the regional Set 4 in stereograms visualizing the data covering all the study area (Fig. 2b). However, regional fractures of Sets 4 and 5 predominantly abut against the NE-SW trending Set 3 fractures, and Set 3 fractures are more continuous with respect to the regional Sets 4 and 5 (Figs. 3d and 4c). Consequently, syn-fault extension fractures of Set 3, kinematically linked with the dextral faults, pre-date the regional fractures of Sets 4 and 5.

Fig. 7e shows the only direct cross-cutting relationship between the sinistral and dextral faults or the associated syn-fault extension

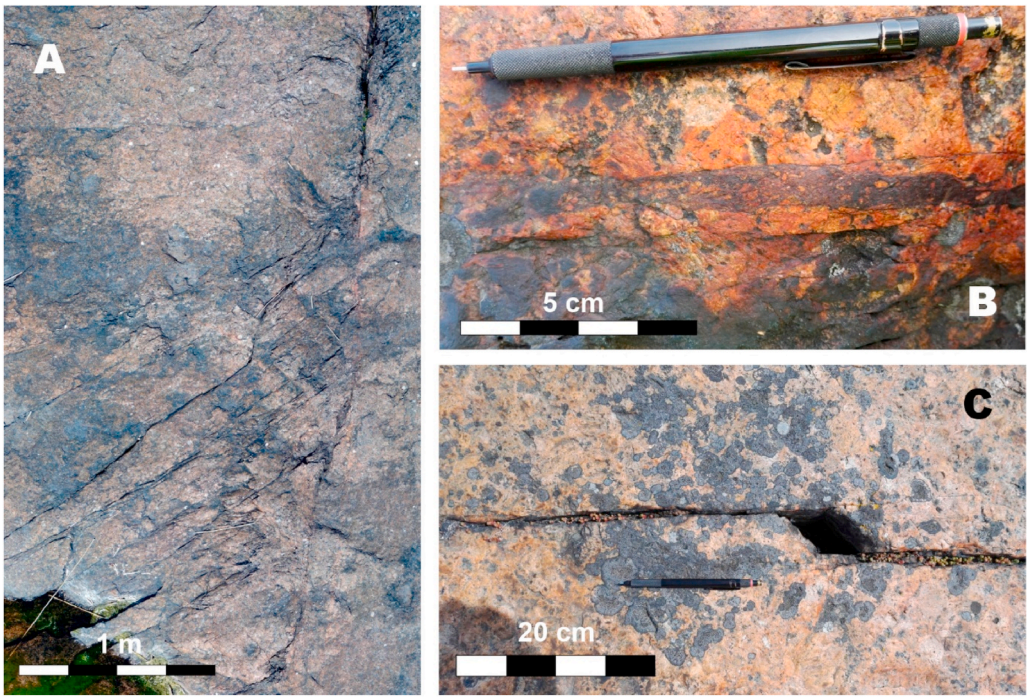

Fig. 6. Field characteristics of the dextral D1 fault. A) Wing-crack fractures in the wall/tip DZ within the southern part of the fault. North is upwards. B) Cataclastic deformation within the fault core. C) A minor pull-apart structure along the secondary slip surface. East is upwards in B and C. *See* Fig. 4c *for the locations of the photos.*

fractures: Minor dextral slip of approximately 3 cm occurred along the eastern slip surface of fault D1 and caused offset of the syn-fault extension fractures of Set 2. This indicates that dextral faulting occurred later than sinistral faulting, but the observed fracture patterns around fault D1 are conflicting with such timing: most NW-SE trending Set 2 extension fractures associated with sinistral faulting terminate against the D1 slip surfaces and hence indicate either synchronous or post-dating, not pre-dating relative timing with respect to dextral faulting. Consequently, we interpret that dextral and sinistral faulting occurred roughly at the same time, prior to the generation of the regional fracture sets, and deformation along the more localized, planar eastern D1 slip surface occurred during a late stage of the faulting event.

4.3.2. Patterns of the regional fractures in spatial association with faults and syn-fault fractures

Comparing the regional fracture sets, the ENE-WSW trending Set 4 occurs largely unaffected across the study area, whereas the orientation and the intensity of the NNW-SSE trending Set 5 is generally more affected by the pre-existing structures. Poor development of Set 5 is observed in areas where sub-parallel fractures pre-existed the Set 5. Such areas include the immediate DZs of the sinistral faults (e.g. Fig. 4a) and domains of pronounced occurrence of the NW-SE trending Set 4 extension fractures (Fig. 8a). Even though the orientation of Set 4 fractures remain relatively unchanged, their localization is still locally affected as shown by the presence of a through-going Set 4 fracture just next to the terminations of the N-S fault and the associated tip-DZ (Fig. 8b). Moreover, Set 4 fractures are locally seen to bend towards right angles when approaching pre-existing fault-induced fractures.

5. Structural interpretation

5.1. Structural synthesis of the faults and the kinematically linked fractures

All the major faults in the area are sub-vertical and associated with sub-horizontal or gently-plunging lineations, compatible with an overall strike-slip faulting domain. The majority of the faults, including the largest S1 fault, display sinistral kinematics as concluded from fracture patterns in their DZs, and indicate that the main principal stress component (σ_1) at the time of faulting had an approximately NW-SE orientation. The NW-SE trending extension fractures (Set 2), kinematically linked to the sinistral faults, occur as the predominant set within an area between S1 and S8 faults. For this reason, we interpret that the area between S8 and the northern termination of S1 is a major extensional left-handed step-over (Fig. 9a). Moreover, we interpret from the presence of a topographic depression and the minor S8 fault, that the N-S trending small bay in the central part of the Orrengrund island, is underlain by a sinistral fault (S9) comparable in size to S1. In this interpretation the sinistral S8 (Fig. 9b) is a lower-order slip surface occurring parallel to the unexposed first-order fault S9.

Analogous to dextral slip along fault D3, the similarly oriented NW-SE (to WNW-ESE) Set 2 extension fractures frequently show evidence for dextral slip along them (Fig. 9b and c). As the slips and DZs related to this dextral faulting are limited, we interpret that it occurred during progressive deformation of the controlling sinistral N-S faults: the NW-SE Set 2 fractures initially formed as extension fractures but were later reactivated as shear fractures, forming a conjugate system with the sinistral N-S faults, compatible with approximately NW-SE –oriented maximum compressive stress σ_1.

Origin of the D1 fault is incompatible with the NW-SE σ_1 orientation responsible for the generation of the dominant sinistral faults. However, field relations indicate that slip along the most prominent dextral slip surface was synchronous with sinistral faulting (Section 4.3.1.). Furthermore, occurrence of the structurally similar but smaller dextral D2 fault on the northern shore of Orrengrund indicate that the dextral features are not isolated and potentially negligible features but need to be addressed within the same dynamic context with the dominant sinistral faults. Consequently, we interpret that D1 and D2 are part of a single segmented dextral zone which has at least 350 m along-strike length, but more limited influence on fracturing with respect to that caused by the sinistral faults. The occurrence of the NE-SW trending (Set 3) fractures kinematically linked to the dextral D1-D2 fault is primarily limited to the closest 100–200 m range from the fault traces. Bearing this in mind, we attribute the generation of faults with opposite shear senses

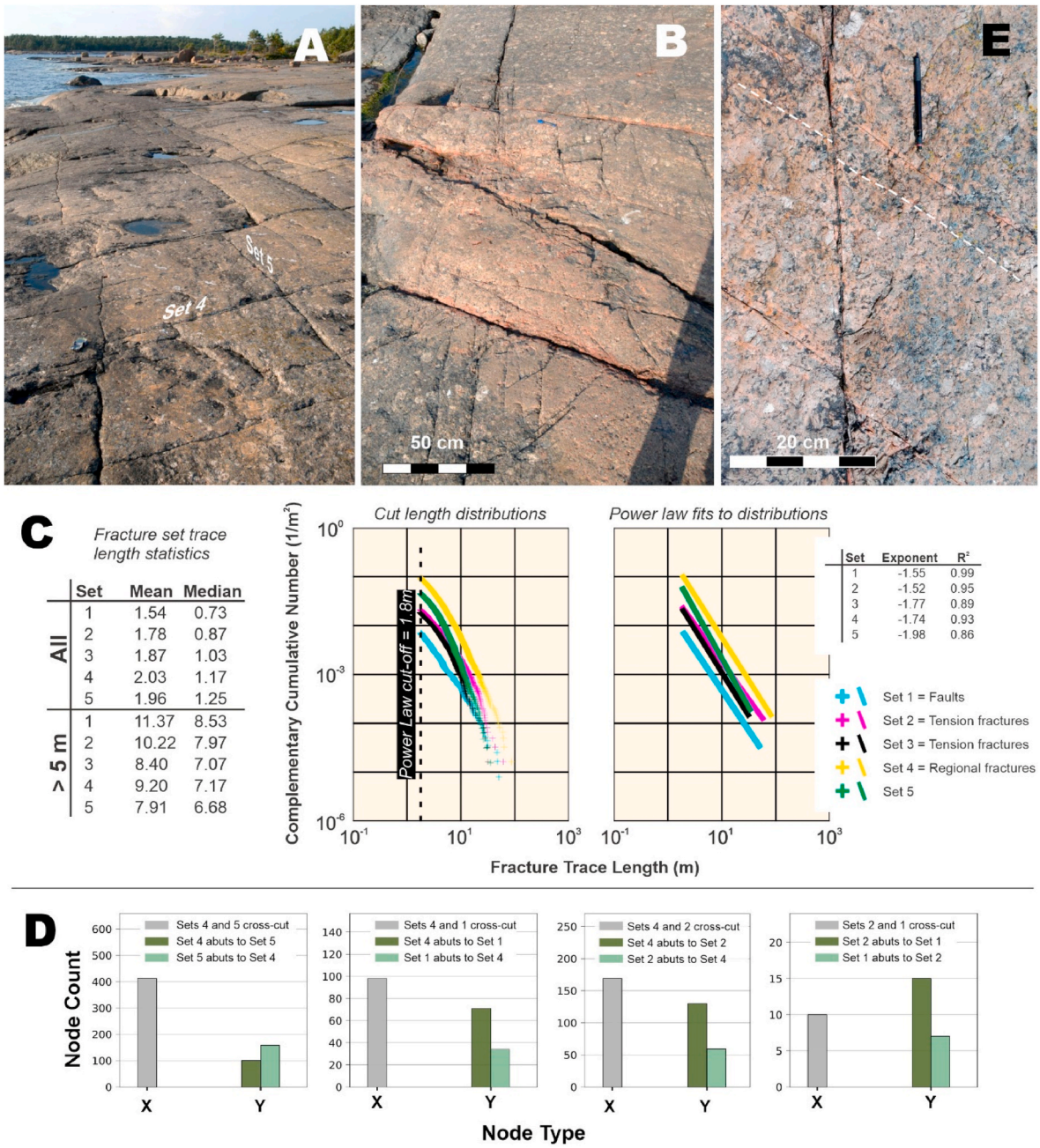

Fig. 7. Relationships between regional and fault-related fractures. A) Mutually cross-cutting and abutting orthogonal fractures belonging to Sets 4 and 5. View towards North. Image width approximately 1.5 m in the front. B) The regional fractures (Set 4; vertical in photo) typically terminate against the faults and fault-parallel fractures (horizontal in photo). View towards ENE. C) Fracture Set length distribution modelling and statistics. Set statistics are shown for all fracture traces and for fractures >5 m in length. Length distributions are modelled individually for each set using a power law trend with a visually determined cut-off of 1.8 m. Power law modelling resulted in varying exponents for Sets indicating different relative proportions of fractures of different lengths. E.g. Set 5 with an exponent of −1.98 has the lowest relative amount of long fractures in comparison to small fractures and Set 2 with an exponent of −1.52 has the highest relative amount of long fractures within their length distributions. D) Topological relationships of selected fracture Sets for > 5 m fractures. The regional Sets 4 & 5 are characterized by a high proportion of mutual cross-cutting (X-nodes) and no tendency towards preferred abutment (approximately equally high green boxes). By contrast, fractures of the regional Set 4 abut against the faults (Set 1) and the syn-fault Set 2 fractures (higher dark green boxes), indicate post-dating relative timing for Set 4. Abutting of Set 2 against Set 1 is compatible with synchronous timing between the faults and DZ fractures. E) NW-SE trending Set 2 fractures displaying an approximately 3 cm offset along the secondary slip surface of the dextral Orrengrund fault. Pen points towards North. *See* Fig. 4 *for the locations of the field photos.* (For interpretation of the references to color in this figure legend, the reader is referred to the Web version of this article.)

to contrasting strain rate between the sinistral and dextral faults during one single deformation event (Dutta and Mukherjee, 2019). This eventually caused a southward movement of the bedrock block bound by the dextral D1-D2 fault and the sinistral faults occurring to the east of it (blue arrow in Fig. 9a).

As demonstrated above, syn-fault fractures (of Sets 2 & 3) related to both sinistral and dextral faults occur systematically at scales much wider scales than the *"normal DZs"*, and result in the presence of "*wide DZs*" up to at least 300 m widths between the segments of approximately N-S trending faults (Fig. 9a; Section 5.2.2.; Fracture domain II).

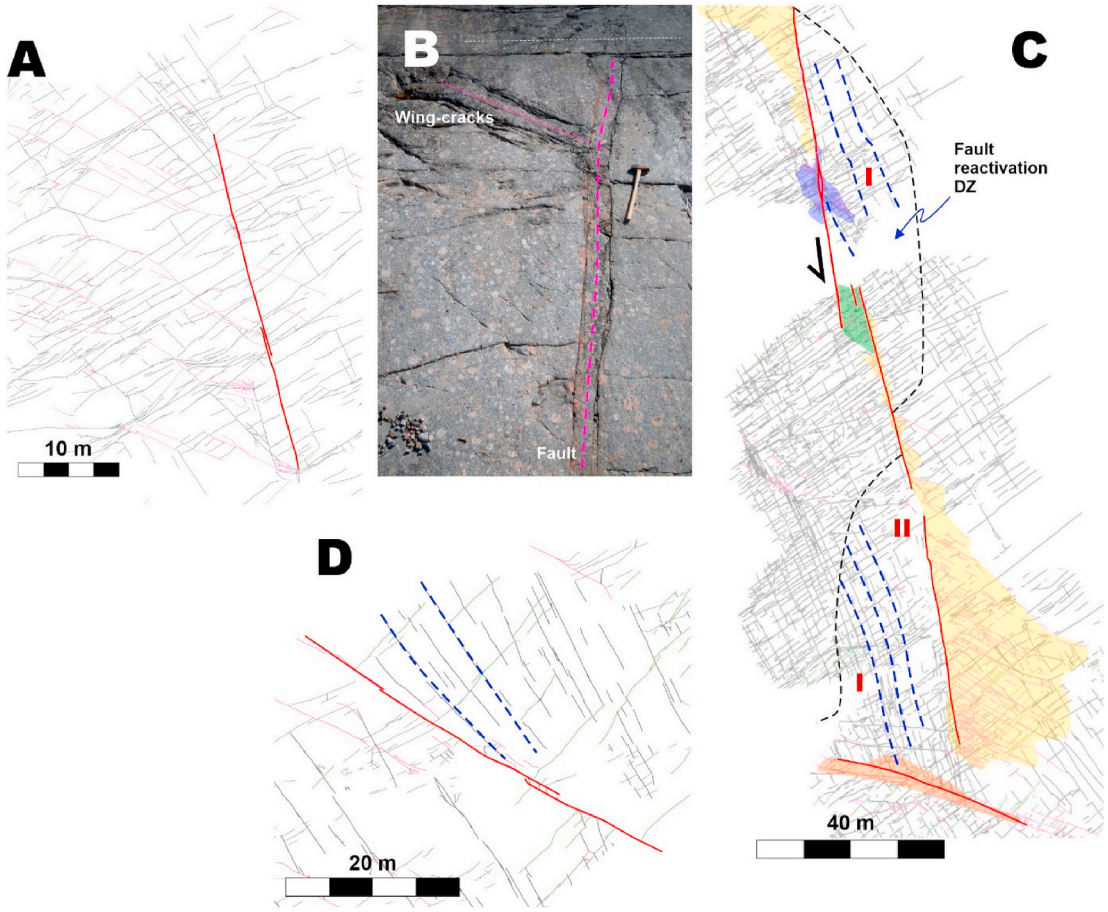

Fig. 8. The effect of the pre-existing fabric upon the overprinting regional fractures. A) The predominance of Set 2 fractures on the western side of the sinistral S5 fault (thick red line) has largely prevented the generation of the subparallel (NNW-SSE) Set 4 fractures. B) Through-going regional fractures (white dashed line in the top of the image) have been localized at the termination of a N-S fault and the associated swarm of wing-cracks. View towards south, hammer length 70 cm. C) A close-up of fault S1 (Fig. 4a) illustrating the deflecting character of Set 4 regional fractures ("I") and the below average fracture intensity ("II") within the fault reactivation damage zones (Section 5.2.1.). D) Defletion of the regional fractures (green and dashed blue) within the vicinity of the shear-reactivated Set 2 fractures (red in image). *See* Fig. 2 *for the locations of figures a,b and d.* (For interpretation of the references to color in this figure legend, the reader is referred to the Web version of this article.)

5.2. Spatial model of fractures

Generation of the ~N-S faults and the kinematically linked syn-fault extension fractures (Section 4.2) resulted in a network of discontinuities which define a specific fault-related structural and mechanical anisotropy within the previously isotropic bedrock of the study area. This anisotropy had a localized controlling effect upon the subsequent regional fractures through development of *fault reactivation DZs* (Section 5.2.1), which in turn contributed to the development of specific fracture domains (Section 5.2.2.) explaining the heterogeneity of fracturing observed in the study area.

5.2.1. Fault reactivation damage zones

An important feature causing deviations in the orientations of regional fractures is the development of *fault reactivation DZs* (Figs. 4a and 8c) in which the later-formed regional fractures show deviation from the characteristic orientations and intensities. The fault reactivation DZs were generated primarily around the larger faults and areas of fault interaction, but also along some dextrally reactivated Set 2 fractures (Fig. 8d). These zones are not homogeneous but show marked asymmetry and along-fault discontinuity, which allows regional fractures to extend all the way to the slip surfaces without any changes in their orientations in many places (Fig. 4a). We attribute the deviations in regional fracture orientation (and intensity) to minor fault reactivation associated with releasing of the regional stresses along faults at the time when the regional fractures were generated, and infer that the development of the fault reactivation DZs follow comparable rock mechanical principles as the regular DZs.

5.2.2. Development of structurally controlled fracture domains

Based on the spatial variation of the fracture patterns, we subdivided the study area into seven fracture domains, whose boundaries are defined by the ~N-S faults and the abrupt changes in the fracture intensity (P21; Dershowitz and Herda, 1992) which occur in spatial connection with long individual fractures (Fig. 10a,d). These individual fractures do stand out on the fracture map due to their lengths but are not associated with any distinct secondary fractures, and, for this reason, were previously not classified as faults (Section 4.2).

Domain I within the southern part of the study area, to the southwest of fault S1, is characterized by the dominance of Set 4 and 5 regional fractures, and the absence of fractures kinematically related to the N-S faults (Fig. 10b). Fractures within ***Domain II*** are dominated by the NW-SE to WNW-ESE trending syn-fault (Set 2) fractures within the major step-over occurring to the west of fault S1. Set 4 is well-developed within this domain, but the pronounced presence of Set 2 fractures has prevented the development of the sub-parallel Set 5 fractures. However, fractures parallel to the NNW-SSE trending Set 5 are present, but they are most commonly associated with small releasing step-overs developed along the dextrally reactivated Set 2 fractures (Section 5.1.; Fig. 9b). Consequently, the NNW-SSE fractures are short and do not

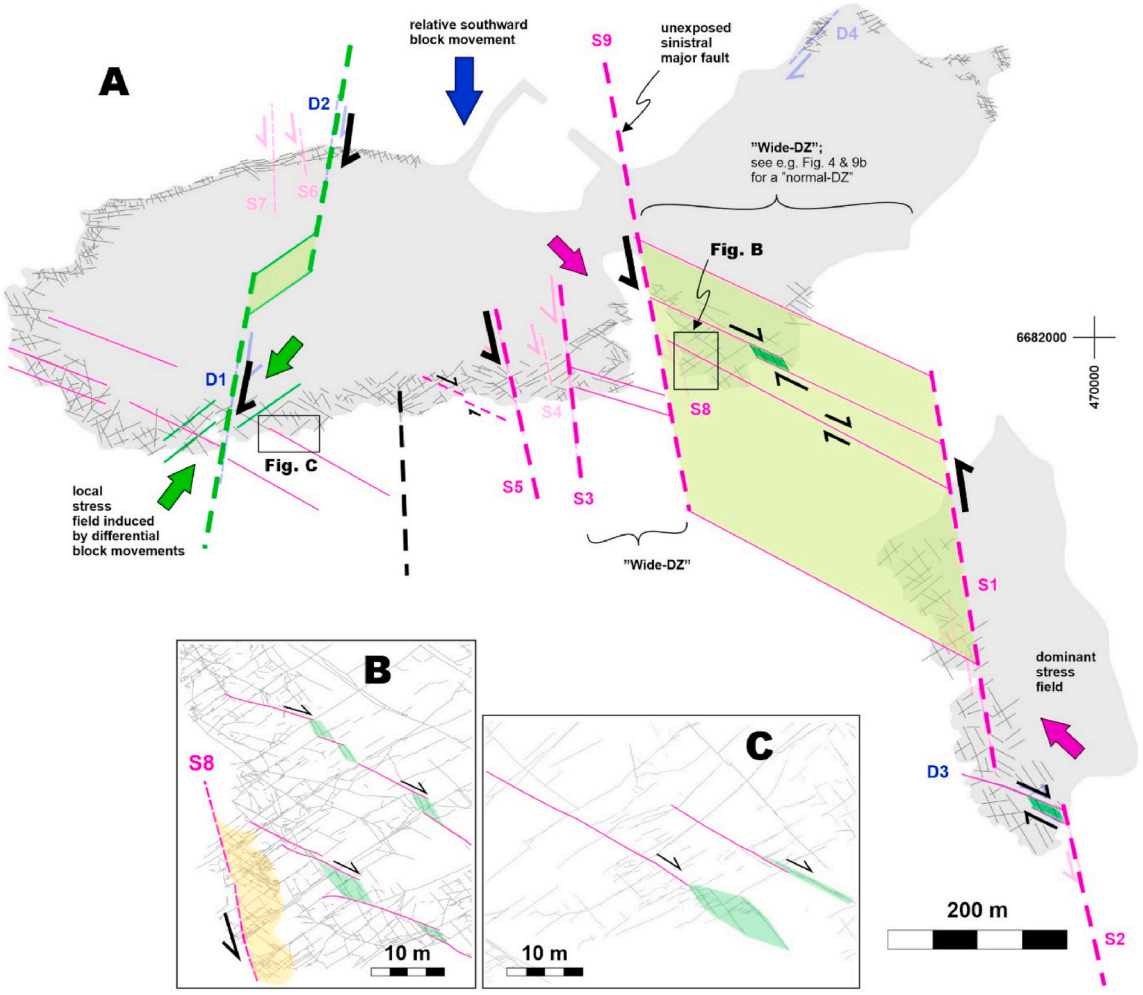

Fig. 9. Structural synthesis of the network of faults and kinematically linked syn-fault fractures, including introduction of the "wide-DZs". A) An interpretation of the network formed by the N-S trending major fault segments, the intervening step-overs (green polygons) and the kinematically linked extension fractures. B) The wall/tip-DZ associated with sinistral S8 fault (yellow polygon) and minor linking DZs (green polygons) developed at right-handed step-overs of dextrally reactivated NW-SE shear fractures. C) Dextral signatures at the terminations of -reactivated NW-SE trending shear fractures. The thin, solid magenta (Set 2) and green (Set 3) lines are extension fractures associated with the sinistral and dextral strike-slip faults, respectively. The thin grey lines are undifferentiated fracture traces, including also regional fractures, and are shown here only for spatial reference. (For interpretation of the references to color in this figure legend, the reader is referred to the Web version of this article.)

define a penetrative fracture fabric comparable to Domain I.

Domain III deviates from the apparently similar domain II with regard to Set 2 fractures which within domain III are less continuous and their occurrence is primarily localized on the western walls of the ~N-S faults. As the ~N-S faults also control the overall fracture intensity (Fig. 10a), we used faults S3, S5 and U1 to subdivide domain III into four sub-domains (IIIa-d). Moreover, we defined the western margin of domain IIId at a large N-S trending Set 1 fracture which is spatially coincident with a distinct change in fracture intensity.

The presence of syn-fault NE-SW (ENE –WSW) trending Set 3 fractures kinematically associated with the zone of dextral faulting (D1-D2) characterize ***Domain IV.*** Together with the more penetrative Set 2 fractures, they define a relatively sparse orthogonal pattern, which occurs at a small angle to another near-orthogonal fracture network defined by the overprinting regional fractures (Sets 4 & 5; Fig. 10c). Sub-domains IVa and IVb share similar fracture orientations but the intensity of fractures is significantly lower in IVa. Set 3 fractures related to dextral faulting within domain IV are recognizable also within sub-domains IIId and IIIc, making the domains III and IV partially overlapping in character (green and magenta bars in Fig. 10a).

The eastern boundary of ***Domain V*** (Fig. 10d) is defined analogously to the domain III/IV -boundary, and the largest difference from domains III and IV is that the dominant fracturing (Set 2) becomes approximately E-W in trend. The regional Set 4 is present while only little direct effect of the ~N-S faults is visible. The overall fracture intensity within this domain is higher than in most other domains. Transition between domains V and VI is gradational and ***Domain VI*** displays a near-orthogonal fracture pattern consisting of two fracture sets trending ENE-WSW and NNW-SSE. Most of the recognized fracture sets are present within ***Domain VII***, but no clear systematics may be recognized due to the small coverage and isolated occurrence of the outcrops within the domain.

6. Discussion

In this investigation we describe a set of sub-vertical strike slip faults with kinematically linked, and subsequent cross-cutting fractures which transect the anorogenic 1.65–1.62 Ga Rapakivi granites in southern Finland. The excellent exposures, mesoscopically isotropic character of the rock and limited fault slips (<20 cm) provide an outstanding possibility to discuss the evolution of the faults and associated damage zones within crystalline rocks, as well as their control over the subsequent fracture patterns. The discussions about the fracture domain-

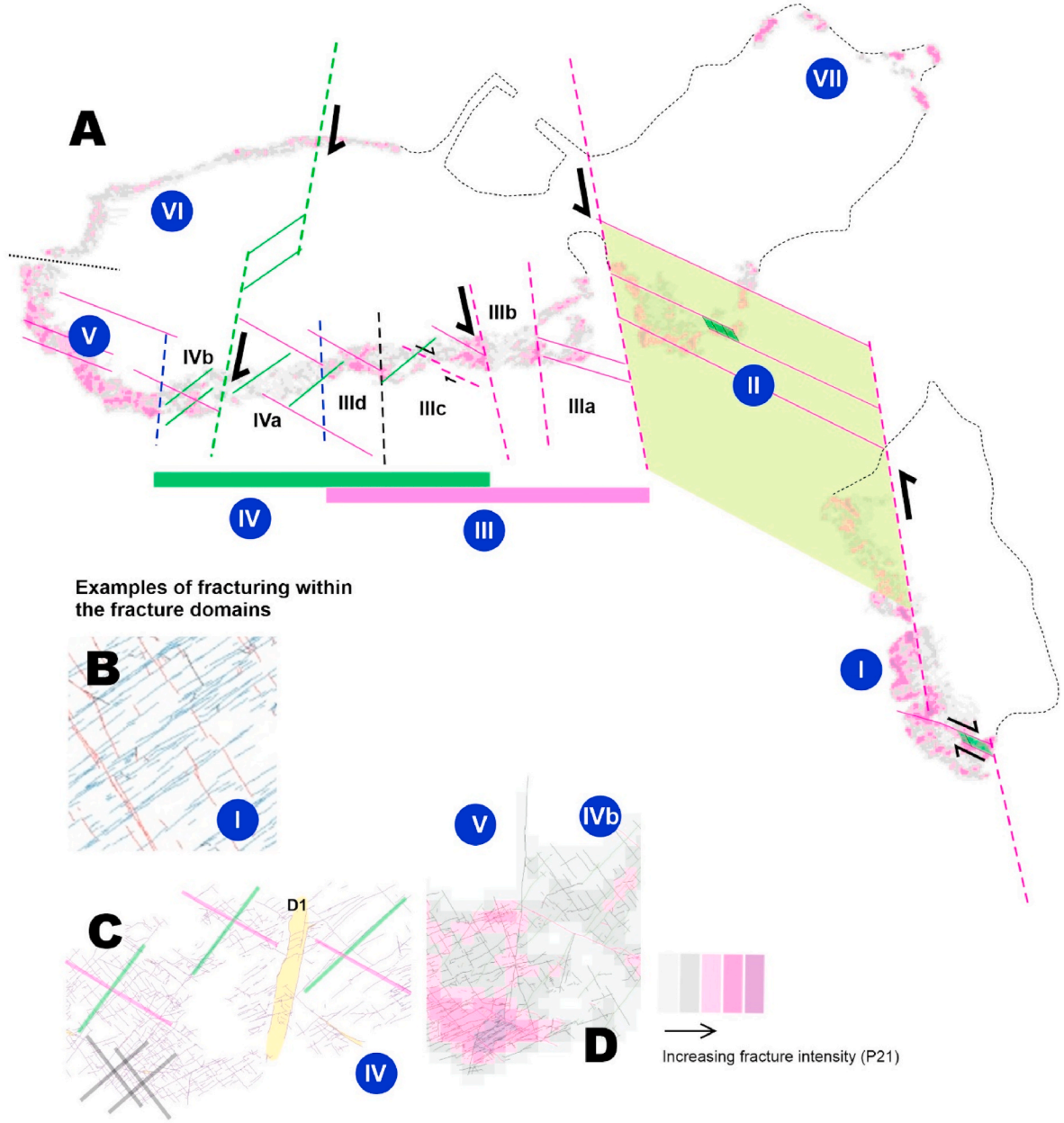

Fig. 10. A) The sub-division of fracture domains utilizing the previously recognized faults (magenta, green and black), as well as new significant rock mechanical discontinuities (blue dashed lines) displaying major influence on the fracture intensity values (P21) B) An example of regional fractures within domain I, largely unaffected by the fault-stage structures. C) Characteristic fracture orientations within domain IV: grey lines = regional fractures, green & magenta = fractures kinematically linked to the N-S faults. D) The drastic change in P21 intensity associated with a long individual N-S fracture consequently use in defining the boundary of the fracture domains IVb and V. (For interpretation of the references to color in this figure legend, the reader is referred to the Web version of this article.)

formation will provide working hypotheses to be tested by forthcoming investigations incorporating rigorous rock mechanical modelling and in-depth analysis of fracture systems within the domains.

6.1. Early evolution of the faults and the associated generation of damage zones

Faults were formed in mesoscopically isotropic, homogeneous host rock and no observable mechanical anisotropy existed during the time of the faulting. Consequently, the formation of damage zones can be directly associated with the faulting and propagation of the fault and associated stress perturbations along the fault or along interacting faults.

According to the general understanding of fault development, DZ widths increase with increasing fault slip, and the thickness of the fault core shows positive correlation with the fault length and slip. However, no universally functioning linear relationship is applicable as the length/slip ratios show a variability of up to two magnitudes depending on e.g. the hosting lithology (Faulkner et al., 2011; Perrin et al., 2016; Scholz, 2019). Due to the variable surface erosion of the margins of the mapped discontinuities exposed on the natural outcrops of this study, leading to apparent apertures, we have no systematic measures for the fault core thicknesses or fracture apertures, and only one unambiguous offset marker (Fig. 7e) was available. For these reasons, we use the i) 2 cm cataclastic breccias observed along the main slip surface of fault D1, and ii) the 3 cm offset along the subsidiary D1 slip surface as minimum values for fault core thickness and slip. Moreover, we use iii) fault S1 in scaling damage zone extent with fault length, as it is the only fault with full exposure of both the trace length and the DZ, and iv) the 5 m wide

wall-DZ of S3 fault in scaling the DZ widths.

The 2 cm core thickness of the D1 fault corresponds to 0.2–2 m slip using the 1:10 to 1:100 ratios applicable to rocks with high to intermediate cohesion (Scholz, 2019). Using the minimum ratio of $D = 10^{-3} L$ (D = displacement, L = length; e.g. Kim and Sanderson, 2005), fault S1 with 180m trace length should have a displacement of 0.18 m, comparable to most conservative estimate (0.2 m) derived from the core thickness vs. displacement relation. According to the scaling relationships between fault displacement and DZ width, (e.g. Scholz, 2019), the 0.18m displacement corresponds to DZ width of approximately 0.18 m, whereas based on the scaling relationship developed for the high-grade rocks of Olkiluoto, SW Finland (Pere et al., 2012), the 2 cm core width indicates a DZ width one magnitude higher, i.e. 2-3 m. Despite the range within the above estimations, the derived 0.18 m and 2–3m DZ widths are compatible to the 60 cm and 5 m width of the core domain and the DZ of fault S3, i.e. the observed values are within the range of variance given by the scaling equations. Another viewpoint into the DZ extent is given by the relationship between the fault length and the tip DZ area required to cover the secondary fractures and faults (Kim and Sanderson, 2005). The approximately 30 × 70 m (width × length) extent of the tip-DZ within the southern termination of fault S1 is well in line with the average of the scaling of Perrin et al. (2016) indicating average lengths of 0.34 and width of 0.09 times the fault length for the tip DZ. However, the scaling equations of Perrin et al. (2016) are not further linked to the fault slip magnitude and, consequently, cannot be used in the evaluation of the slip magnitude. Despite the uncertainties, the limited fault scaling measures (above) appear useful as they show that the fault slip magnitudes were very limited and, together with the poor development of continuous wall-DZs, indicate that the preserved structural signatures relate to an incipient stage of fault evolution.

The extent of the "wide DZs" - defined by the continuous fault-related fractures occurring between the N-S faults of this investigation - may not be explained by the displacement magnitude along the bounding faults. The development of DZ widths of larger than 100 m would require displacements of over 100 m, and kilometers to tens of kilometers long faults (Faulkner et al., 2011; Scholz, 2019). Since DZs widths, after a threshold range of a few hundred meters, do not grow significantly (Scholz, 2019), wide DZs could possibly result from the interactions of several faults (Kim et al., 2004; Peacock et al., 2017), typically leading to heterogeneous fracture intensity distributions (Ostermeijer et al., 2020). An example of exceptionally wide DZs are found within the Ordovician carbonates of the Tarim Basin, where the observed DZ had widths up to 3.5 km (Ma et al., 2019; Wan et al., 2016). Wu et al. (2019) attributed the wide DZs to the superimposing effect of several faults, including outward growth of secondary faults. However, slips of several hundreds to thousands of meters along the up to 70 km long master strike-slip faults (Wu et al., 2019) are still within the magnitude of the scaling laws (op. cit.) and hence not comparable to the extreme 1:1 DZ width vs. individual fault segment length (S1) relationship associated with the "wide-DZs" noted in this investigation. The overall lack of fault-related Y- and P-fractures within the area of this study is in line with the small observed displacement magnitudes due to which the formation of wall damage zone has not progressed very far. This further indicates that the formation of the "wide DZs" is the result of interactions between the fault segments and associated stress perturbations.

Earlier in this paper, we attributed fault-induced fracturing within Fracture domain II to the presence of a large pull-apart structure between faults S1 and S9. This origin is comparable to the development of type I tension veins between two parallel fault segments along fault S3 ("BSF in Fig. 5d), or within pull-apart basins of overlapping geometries (Corti et al., 2020; Corti and Dooley, 2015; Dooley and McClay, 1997; Kim et al., 2004). Based on the wide extent of the syn-fault fractures (Set 2 & 3) across fracture domain V, we infer that the faulting-stage involved multiple discontinuous N-S faults that were kinematically linked across wide distances with respect to the length of the individual fault segments, and the resulting fracture patterns markedly exceed any existing scaling laws.

6.2. Fracture domain subdivision

A pre-existing fabric will typically contribute to the development of the cross-cutting fractures (Amadei, 1996), but the question of mechanical anisotropy is more complex as for a discontinuity (fault/-fracture) to affect the origin and orientation of later fractures, there needs to be a stress perturbation at that location. This further means that at the time of the formation of the regional fractures, the faults were reactivated and were thus in orientation optimal for reactivation with respect to the prevailing stress state. In this study, the mechanical anisotropy is characterized by the N-S faults and the kinematically associated syn-fault extension fractures, and hence contrasting to the non-tectonic origins of fractures in crystalline rocks arising from thermal processes within cooling intrusions (Crider, 2015; Pollard and Aydin, 1990; Sanders et al., 2003; Segall and Pollard, 1983; Yuguchi et al., 2012). Further, recognition of the "fault reactivation DZs" (Section 5.2.1.; Fig. 4a) indicates that the reactivation of the faults exerted major control upon the development of the overprinting fractures. Consequently, we evaluate the fracture domain sub-division (Section 5.2.2.) in the scale of faults-bound blocks, as fracture properties in general (Ovaskainen, 2020), and specifically in the case of structural inheritance are not scale-invariant (Samsu et al., 2020).

The validity of the fracture domain sub-division, which is based on visual judgement and fracture intensity (P21), is supported by the contrasts within the fracture connectivity (Fig. 11a and b) and orientation (Fig. 11c) between the defined domains. Fracture connectivity within the domains is visualized with the connections per branch parameter and node proportion plots are shown for all domains (Manzocchi, 2002; Sanderson and Nixon, 2015). No marked differences exist in the fracture connectivity between domains I and II, but the two-peak orientation cluster of the ~NW-SE fractures in domain II clearly indicate the dominance of Set 5 fractures for domain II and also validates the subdivision between domains I and II. The connections per branches values between the neighboring sub-domains IIIa-d and IVa-b, located outside the major sinistral step-over (Fig. 9), show marked contrasts (value range 1.25–1.55; Fig. 11a). The exception is the similarity of sub-domains IIIa and b. However, Set 2 fractures in IIIa are continuous and penetrative, but in IIIb they are clearly spatially associated to the N-S faults in (App. 1). In general, there is a progressive increase of ~NW-SE (Set 2 + 5) fractures from IIIb to IIId. In domains IVa and IVb the ~NE-SW and ~NW-SE fractures occur in approximately equal proportions and the two-peak orientation pattern of the NE-SW and NW-SE fractures in stereographic projections support the presence of two separate orthogonal pairs of fracture sets (regional Sets 4 & 5; syn-fault Sets 2 & 3; Fig. 11c). Fractures within all the defined domains are relatively clustered within the XYI-topology plot (Fig. 11b). Outliers include domains IVa,b and IIIb, which stand out through the relatively low proportion of Y-nodes, and domain V, with higher proportion of the Y-nodes. The orientation distributions of domains V, VI and VII clearly deviate from all the remaining domains and support the conducted domain subdivision.

Our findings over the relationship of the faults and syn-fault fractures (Sections 4.2., 4.3.) are in line with increasing fracture frequency and increase heterogeneity of fracture densities towards the faults (Ostermeijer et al., 2020; Torabi et al., 2018). Our results further highlight that faults and synchronous fractures additionally provide a major contribution towards defining the patterns of the later-formed fractures, and hence the overall architecture of the brittle structures that developed in the initially isotropic crystalline crust.

6.3. Regional correlation

The strike-slip regime responsible for faulting described in this paper (Section 5.1.), characterized by NW-SE main principal stress component

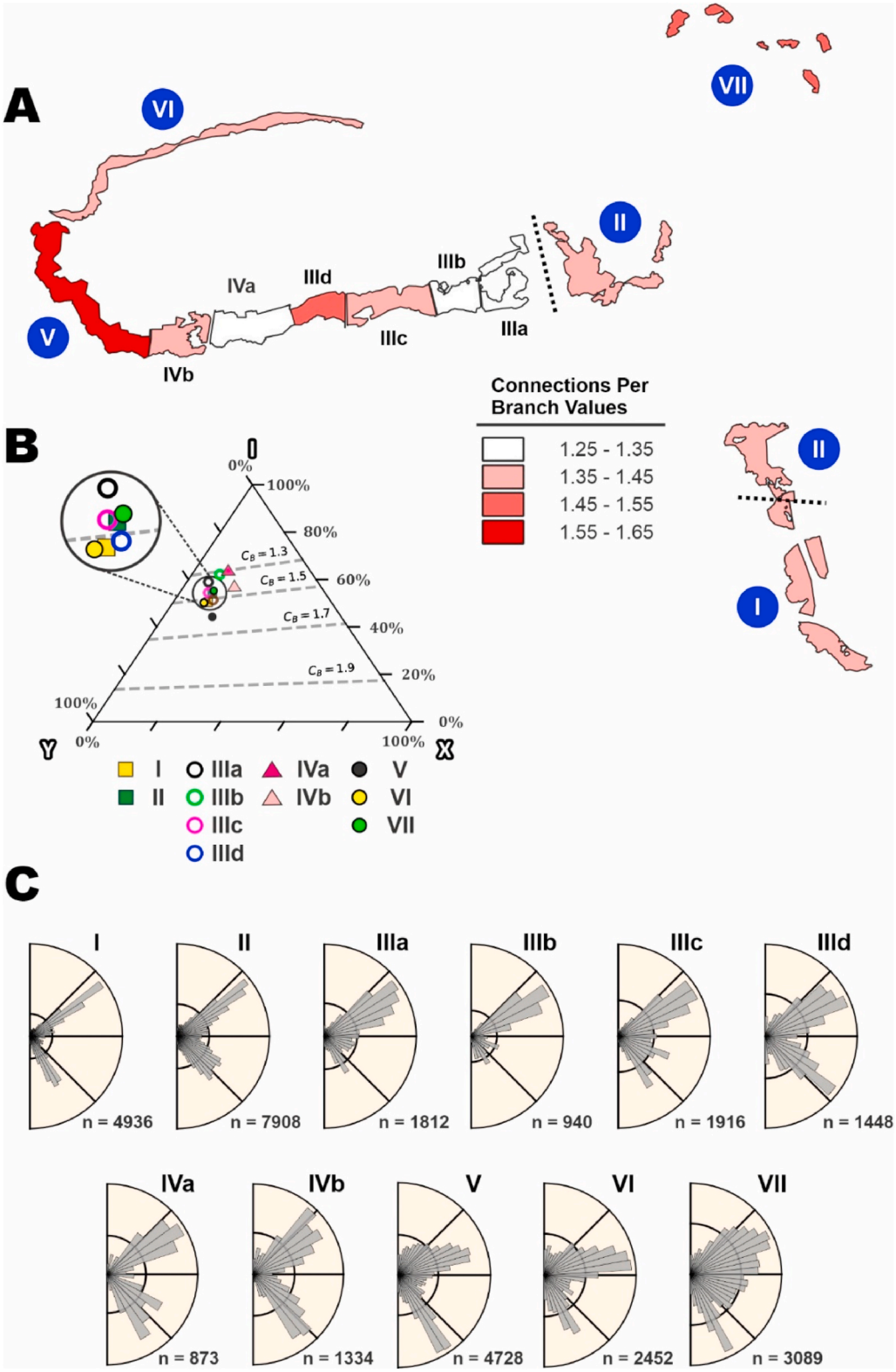

Fig. 11. Fracture analyses to evaluate the validity of the fracture domains subdivision. Fractures within the "normal DZs"is excluded from the analyses. A) Colormap visualizing the connections per branch topological parameter (Sanderson and Nixon, 2015) *for all fracture domains. B) Ternary figure of topological X-, Y- and I-node proportions* (Manzocchi, 2002) *of fracture domains including the connections per branch parameter values as contours. Both the node proportions and connectivity per branch values are scalar measures of the connectivity of a fracture network. X-nodes signify crosscuts between fractures, Y-nodes abutments and I-nodes isolated terminations and the proportions of each node type can be used to interpret the fracture pattern of a network which directly affects connectivity i.e., how fractures connect to each other. Connections per branch is a scalar value calculated from the node proportions. C) Length-weighted equal-area rose plots* (Sanderson and Peacock, 2020) *of fracture domain traces.*

(σ_1) is compatible with the stress field attributed to the sinistral slip along the N-S trending faults and the origin of the associated NNW-SSE trending fractures in the Helsinki region (Fig. 1; Elminen et al., 2008). No absolute timing constraints for these strike-slip faults are available, but they post-date the ductile dextral reactivation of the NE trending Porkkala-Mäntsälä shear zone (PMSZ; Fig. 1a), which is correlated with the crystallization of the 1.64 Ga (Vaasjoki, 1977) Obbnäs and Bodom Rapakivi plutons, (Elminen et al., 2008; Heeremans and Wijbrans, 1999; Kosunen, 1999). Potential association of the strike-slip zones of the Orrengrund-Båksören area and the similarly oriented NNW-SSE and NNE-SSW trending polymetallic In-bearing greisen veins within the western parts of the Wiborg batholith (Broman et al., 2018; Valkama et al., 2016) points towards a timing around the end of the crystallization of the Wiborg batholith (1.62 Ga; Rämö and Haapala, 2005).

However, since structural characterisation of the polymetallic vein systems is unavailable, it is possible that these veins pre-date the strike-slip faults, and the two are instead associated to the same crustal-scale N-S trending weakness zones underlying the Wiborg Batholith (Korja and Heikkinen, 1995). It is also possible that coalescence of systematically arranged Mode I microcracks (Anders et al., 2014), unrecognized in field studies, defines a weakness orientation that controlled the growth of the recognized N-S faults.

The NW-SE extension at 1.56 Ga interpreted for the Olkiluoto area in SW Finland from diabase dykes and fault slip data (Fig. 1; Stage 3 by Mattila and Viola, 2014) is incompatible with the paleostress orientations responsible for strike-slip faulting of this study. However, eigenvector analysis of the 1.55–1.37 Ga, NNW-SSE and ENE-WSW trending greisen veins in the Olkiluoto area (Southwestern Finland) and opening of the approximately coeval NW-SE trending Satakunta graben (15 km NE of Eurajoki; Kohonen et al., 2003) point towards extensional to transtensional faulting with an NE-SW oriented σ_3 roughly around 1.6–1.3 Ga (Mattila and Viola, 2014). Moreover, partitioning of the overall NE-SW extension during intracratonic Mesoproterozoic rifting has been discussed as a potential reason for the generation of the N-S and E-W trending belts of Rapakivi magmatism (Ripa and Stephens, 2020). As far as this work is concerned, NE-SW extension under an overall transtensional setting is compatible with the generation of the strike-slip faults of the Orrengrund-Båksören area, and could also explain the extreme extent of the "wide DZs" associated with the N-S strike-slip faults (Section 5.1). However, better constraints for the fault timing are required.

7. Conclusions

- A set of approximately N-S trending, dominantly sinistral subvertical strike-slip faults transect the ca. 1.65 Ga Rapakivi granites in Loviisa, southern Finland
- Well-developed fault damage zones indicate i) limited offsets (<20 cm) along the faults, preserving structures related to the incipient stage of faulting, and ii) fault-generation in mesoscopically isotropic material devoid of any pre-existing fabrics
- Two sets of mutually synchronous regional fractures post-date the faults and the kinematically linked syn-fault extension fractures
- Fault evolution defines four separate but partially overlapping features which collectively govern the character of fractures of the study area. Two of these relate to faulting, and two to the release of regional stresses along faults during the subsequent generation of regional fractures:
  - o *The faulting event* is characterized by 1) normal damage zones (DZ) within the immediate vicinity of the faults, and 2) wider DZs in-between parallel to sub-parallel fault segments through generation of syn-fault fractures kinematically linked with the N-S strike-slip faults. Some of these wide DZs are associated with 100m-scale step-overs of the sinistral faults.
  - o *The structural control of the syn-fault fractures over the later-formed regional fractures* resulted in 3) narrow "fault reactivation DZs" within the immediate vicinity of the faults and fault intersections, as revealed by deviations within the orientation or intensity of the regional fractures, and 4) fault-bound fracture domains in which the pre-existing structural anisotropy (introduced during the faulting stage) and stress release along faults governed the development of the regional fractures. Of particular importance is the intensity of the fault-stage structures which inhibited the development of the sub-parallel NNW-SSE trending Set 5 regional structures, best exemplified within an approximately 300 m-scale step-over between segments of sinistral faults

Declaration of competing interest

The authors declare that they have no known competing financial interests or personal relationships that could have appeared to influence the work reported in this paper.

Acknowledgements

We acknowledge National Nuclear Waste Management Fund (Finland) for funding the KARIKKO and MIRA-3D projects; Mathias Lauraeus, Ismo Aaltonen och Henrik Wik for assistance in trace line digitization, comments on the manuscript by Prof. Atle Rotevatn and the reviews by the Journal Editor Stephen Laubach and the officially appointed Journal Reviewers Santau Misra and Jess McBeck which all helped to improve the manuscript.

Appendix A. Supplementary data

Supplementary data to this article can be found online at https://doi.org/10.1016/j.jsg.2021.104304.

Electronic appendices

Appendix 1Trace map over all the fractures and faults of the Orrengrund-Båksören study area

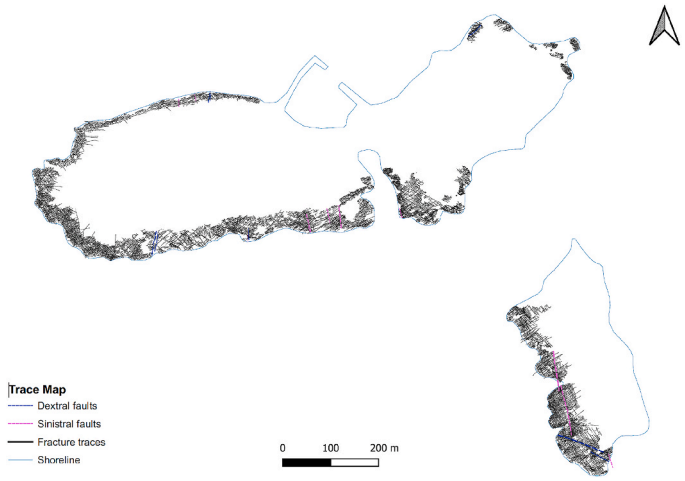

App. 1.

Appendix 2Orthophotograph of the study area (A snapshot of both appendices is provided below)

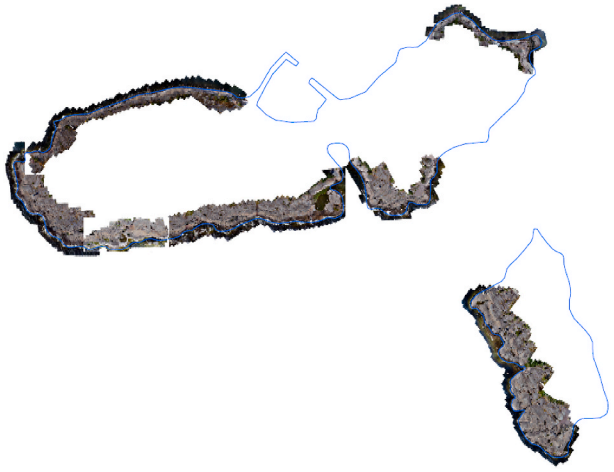

App. 2.

References

Amadei, B., 1996. Importance of anisotropy when estimating and measuring in situ stresses in rock. Int. J. Rock Mechan. Min. Sci. Geomechan. 33 (3), 293–325. https://doi.org/10.1016/0148-9062(95)00062-3.

Anders, M.H., Laubach, S.E., Scholz, C.H., 2014. Microfractures: a review. J. Struct. Geol. 69 (PB), 377–394. https://doi.org/10.1016/j.jsg.2014.05.011.

Bazalgette, L., Petit, J.P., Amrhar, M., Ouanaïmi, H., 2010. Aspects and origins of fractured dip-domain boundaries in folded carbonate rocks. J. Struct. Geol. 32 (4), 523–536. https://doi.org/10.1016/j.jsg.2010.03.002.

Behrestagni, M., Sehizadeh, M., Young, R., 2018. ONKALO POSE Experiment - Integrated Analyses of True- T Ri a Xial Tests. 31(June).

Bonnet, E., Bour, O., Odling, N.E., Davy, P., Main, I., Cowie, P., Berkowitz, B., 2001. Scaling of fracture systems in geological media. Rev. Geophys. 39 (3), 347–383.

Bose, N., Dutta, D., Mukherjee, S., 2020. Refraction of micro-fractures due to shear-induced mechanical stratigraphy in a low-grade meta-sedimentary rock. J. Struct. Geol. 133 (August 2019), 103995. https://doi.org/10.1016/j.jsg.2020.103995.

Broman, C., Sundblad, K., Valkama, M., Villar, A., 2018. Deposition conditions for the indium-bearing polymetallic quartz veins at Sarvlaxviken, south-eastern Finland. Mineral. Mag. 82 (S1), S43–S59. https://doi.org/10.1180/minmag.2017.081.024.

Carlini, M., Viola, G., Mattila, J., Castellucci, L., 2019. The role of mechanical stratigraphy on the refraction of strike-slip faults. Solid Earth 10 (1), 343–356. https://doi.org/10.5194/se-10-343-2019.

Choi, J.H., Edwards, P., Ko, K., Kim, Y.S., 2016. Definition and classification of fault damage zones: a review and a new methodological approach. Earth Sci. Rev. 152, 70–87. https://doi.org/10.1016/j.earscirev.2015.11.006.

Corti, G., Dooley, T.P., 2015. Lithospheric-scale centrifuge models of pull-apart basins. Tectonophysics. https://doi.org/10.1016/j.tecto.2015.09.004.

Corti, G., Nencini, R., Skyttä, P., 2020. Modelling the influence of pre-existing brittle fabrics on the development and architecture pull-apart basins. J. Struct. Geol. 131 https://doi.org/10.1016/j.jsg.2019.103937. July 2019.

Crider, J.G., 2015. The initiation of brittle faults in crystalline rock. J. Struct. Geol. 77, 159–174. https://doi.org/10.1016/j.jsg.2015.05.001.

Davy, P., Le Goc, R., Darcel, C., Bour, O., De Dreuzy, J.R., Munier, R., 2010. A likely universal model of fracture scaling and its consequence for crustal hydromechanics. J. Geophys. Res.: Solid Earth 115 (10), 1–13. https://doi.org/10.1029/2009JB007043.

Dershowitz, W.S., Herda, H.H., 1992. Interpretation of fracture spacing and intensity. In: The 33rd U.S. Symposium on Rock Mechanics (USRMS), vol. 10. https://www.onepetro.org/conference-paper/ARMA-92-0757.

Dooley, T., McClay, K., 1997. Analogue modelling of pull-apart basins. AAPG (Am. Assoc. Pet. Geol.) Bull. 81 (66), 1804–1826.

Douma, L.A.N.R., Regelink, J.A., Bertotti, G., Boersma, Q.D., Barnhoorn, A., 2019. The mechanical contrast between layers controls fracture containment in layered rocks. J. Struct. Geol. 127 (June), 103856. https://doi.org/10.1016/j.jsg.2019.06.015.

Dutta, D., Mukherjee, S., 2019. Opposite shear senses: geneses, global occurrences, numerical simulations and a case study from the Indian western Himalaya. J. Struct. Geol. 126 (June), 357–392. https://doi.org/10.1016/j.jsg.2019.05.008.

Elminen, T., Airo, M.L., Niemelä, R., Pajunen, M., Vaarma, M., Wasenius, P., Wennerström, M., 2008. Fault structures in the Helsinki area, southern Finland. Spec. Pap. Geol. Surv. Finland 185–213. *2008(47)*.

English, J., 2012. Thermomechanical origin of regional fracture systems. AAPG (Am. Assoc. Pet. Geol.) Bull. 96 (9), 1597–1625. https://doi.org/10.1306/01021211018.

Faulkner, D.R., Mitchell, T.M., Jensen, E., Cembrano, J., 2011. Scaling of fault damage zones with displacement and the implications for fault growth processes. J. Geophys. Res. 116 (B5), B05403. https://doi.org/10.1029/2010JB007788.
Fossen, H., 2016. *Structural Geology* (2 Nd Editi). Cambridge University Press.
Griffith, A.A., 1921. VI. The phenomena of rupture and flow in solids. Philos. Trans. R. Soc. Lond. - Ser. A Contain. Pap. a Math. or Phys. Character 221 (582–593), 163–198. https://doi.org/10.1098/rsta.1921.0006.
Haapala, I., Rämö, O.T., 1992. Tectonic setting and origin of the Proterozoic rapakivi granites of southeastern Fennoscandia. Trans. R. Soc. Edinb. Earth Sci. 83 (1–2), 165–171. https://doi.org/10.1017/S0263593300007859.
Heeremans, M., Wijbrans, J., 1999. Late Proterozoic tectonic events in southern Finland, constrained by 40Ar/39Ar incremental heating and single spot fusion experiments on K-feldspars. Terra. Nova 11 (5), 216–222. https://doi.org/10.1046/j.1365-3121.1999.00250.x.
Karell, F., Ehlers, C., Airo, M.L., 2014. Emplacement and magnetic fabrics of rapakivi granite intrusions within Wiborg and Åland rapakivi granite batholiths in Finland. Tectonophysics 614, 31–43. https://doi.org/10.1016/j.tecto.2013.12.006.
Kim, Y.S., Peacock, D.C.P., Sanderson, D.J., 2004. Fault damage zones. J. Struct. Geol. 26 (3), 503–517. https://doi.org/10.1016/j.jsg.2003.08.002.
Kim, Y.S., Sanderson, D.J., 2005. The relationship between displacement and length of faults: a review. Earth Sci. Rev. 68 (3–4), 317–334. https://doi.org/10.1016/j.earscirev.2004.06.003.
Kohonen, J., Ojala, V.~J., Sorjonen-Ward, P., 2003. Distribution of Sedimentary Cover within the Central Fennoscandian Shield: Depositional Basins or Selective Preservation. EGS - AGU - EUG Joint Assembly, p. 13995.
Korja, A., Heikkinen, P.J., 1995. Proterozoic extensional tectonics of the central fennoscandian Shield: results from the baltic and bothnian echoes from the lithosphere experiment. Tectonics 14 (2), 504–517. https://doi.org/10.1029/94TC02905.
Kosunen, P., 1999. THE RAPAKIVI GRANITE PLUTONS of BODOM and OBBNAS , SOUTHERN FINLAND : PETROGRAPHY and GEOCHEMISTRY Diabase Rapakivi Granite Granite Metabasalt and Amphibolite Phyllite , Mica Schist , and Mica Gneiss Quartz-Feldspar Schist and Gneiss.
Kranz, R.L., 1983. Microcracks in rocks: a review. Tectonophysics 100 (1–3), 449–480. https://doi.org/10.1016/0040-1951(83)90198-1.
La Bruna, V., Lamarche, J., Agosta, F., Rustichelli, A., Giuffrida, A., Salardon, R., Marié, L., 2020. Structural diagenesis of shallow platform carbonates: role of early embrittlement on fracture setting and distribution, case study of Monte Alpi (Southern Apennines, Italy). J. Struct. Geol. 131, 103940. https://doi.org/10.1016/j.jsg.2019.103940. June 2019.
Laubach, S.E., Lander, R.H., Criscenti, L.J., Anovitz, L.M., Urai, J.L., Pollyea, R.M., Hooker, J.N., Narr, W., Evans, M.A., Kerisit, S.N., Olson, J.E., Dewers, T., Fisher, D., Bodnar, R., Evans, B., Dove, P., Bonnell, L.M., Marder, M.P., Pyrak-Nolte, L., 2019. The role of chemistry in fracture pattern development and opportunities to advance interpretations of geological materials. Rev. Geophys. 57 (3), 1065–1111. https://doi.org/10.1029/2019RG000671.
Lavenu, A.P.C., Lamarche, J., 2018. What controls diffuse fractures in platform carbonates? Insights from Provence (France) and Apulia (Italy). J. Struct. Geol. https://doi.org/10.1016/j.jsg.2017.05.011.
Luosto, U., Tiira, T., Korhonen, H., Azbel, I., Burmin, V., Buyanov, A., Kosminskaya, I., Ionkis, V., Sharov, N., 1990. Crust and upper mantle structure along the DSS Baltic profile in SE Finland. Geophys. J. Int. 101 (1), 89–110. https://doi.org/10.1111/j.1365-246X.1990.tb00760.x.
Ma, D.B., Wu, G.H., Scarselli, N., Luo, X.S., Han, J.F., Chen, Z.Y., 2019. Seismic damage zone and width–throw scaling along the strike-slip faults in the Ordovician carbonates in the Tarim Basin. Petrol. Sci. 752–762. https://doi.org/10.1007/s12182-019-0352-4.
Mancktelow, N.S., Pennacchioni, G., 2005. The control of precursor brittle fracture and fluid-rock interaction on the development of single and paired ductile shear zones. J. Struct. Geol. 27 (4), 645–661. https://doi.org/10.1016/j.jsg.2004.12.001.
Manda, A.K., Mabee, S.B., Wise, D.U., 2008. Influence of rock fabric on fracture attribute distribution and implications for groundwater flow in the Nashoba Terrane, eastern Massachusetts. J. Struct. Geol. 30 (4), 464–477. https://doi.org/10.1016/j.jsg.2007.12.006.
Manzocchi, T., 2002. The connectivity of two-dimensional networks of spatially correlated fractures. Water Resour. Res. 38 (9), 1–20. https://doi.org/10.1029/2000wr000180.
Mattila, J., Viola, G., 2014. New constraints on 1.7Gyr of brittle tectonic evolution in southwestern Finland derived from a structural study at the site of a potential nuclear waste repository (Olkiluoto Island). J. Struct. Geol. 67 (PA), 50–74. https://doi.org/10.1016/j.jsg.2014.07.003.
McCaffrey, K.J.W., Sleight, J.M., Pugliese, S., Holdsworth, R.E., 2003. Fracture Formation and Evolution in Crystalline Rocks: Insights from Attribute Analysis, vol. 214. Geological Society Special Publication, pp. 109–124. https://doi.org/10.1144/GSL.SP.2003.214.01.07. May 2014.
Nejati, M., Aminzadeh, A., Amann, F., Saar, M.O., Driesner, T., 2020. Mode I fracture growth in anisotropic rocks: theory and experiment. Int. J. Solid Struct. 195, 74–90. https://doi.org/10.1016/j.ijsolstr.2020.03.004.
Nironen, M., 1997. The Svecofennian Orogen: a tectonic model. Precambrian Res. 86 (1–2), 21–44. https://doi.org/10.1016/S0301-9268(97)00039-9.
Nyberg, B., Nixon, C.W., Sanderson, D.J., 2018. NetworkGT: a GIS tool for geometric and topological analysis of two-dimensional fracture networks. Geosphere 14 (4), 1618–1634. https://doi.org/10.1130/GES01595.1.
Okko, O., Front, K., Anttila, P., 2003. Low-angle fracture zones in rapakivi granite at Hästholmen, Southern Finland. Eng. Geol. 69 (1–2), 171–191. https://doi.org/10.1016/S0013-7952(02)00281-8.
Ostermeijer, G.A., Mitchell, T.M., Aben, F.M., Dorsey, M.T., Browning, J., Rockwell, T.K., Fletcher, J.M., Ostermeijer, F., 2020. Damage zone heterogeneity on seismogenic faults in crystalline rock; a field study of the Borrego Fault, Baja California. J. Struct. Geol. 137 (August 2019), 104016. https://doi.org/10.1016/j.jsg.2020.104016.
Ovaskainen, N., 2020. Nikolas Ovaskainen Scalability of Lineament and Fracture Networks within the Crystalline Wiborg Rapakivi Batholith. SE Finland M aster ' s Thesis Turku 2020.
Peacock, D.C.P., 2001. The temporal relationship between joints and faults. J. Struct. Geol. 23 (2–3), 329–341. https://doi.org/10.1016/S0191-8141(00)00099-7.
Peacock, D.C.P., Dimmen, V., Rotevatn, A., Sanderson, D.J., 2017. A broader classification of damage zones. J. Struct. Geol. 102, 179–192. https://doi.org/10.1016/j.jsg.2017.08.004.
Peacock, D.C.P., Nixon, C.W., Rotevatn, A., Sanderson, D.J., Zuluaga, L.F., 2016. Glossary of fault and other fracture networks. J. Struct. Geol. 92, 12–29. https://doi.org/10.1016/j.jsg.2016.09.008.
Pere, T., Aro, S., Mattila, J., Ahokas, H., Vaittinen, T., 2012. Layout Determining Features , Their Influence Zones and Respect Distances at the Olkiluoto Site, vol. 31. Issue December.
Perrin, C., Manighetti, I., Gaudemer, Y., 2016. Off-fault tip splay networks: a genetic and generic property of faults indicative of their long-term propagation. Compt. Rendus Geosci. 348 (1), 52–60. https://doi.org/10.1016/j.crte.2015.05.002.
Petford, N., 2003. Controls on Primary Porosity and Permeability Development in Igneous Rocks. Geological Society Special Publication. https://doi.org/10.1144/GSL.SP.2003.214.01.06.
Phillips, T.B., Fazlikhani, H., Gawthorpe, R.L., Fossen, H., Jackson, C.A.L., Bell, R.E., Faleide, J.I., Rotevatn, A., 2019. The influence of structural inheritance and multiphase extension on rift development, the NorthernNorth Sea. Tectonics 38 (12), 4099–4126. https://doi.org/10.1029/2019TC005756.
Pollard, D.D., Aydin, A., 1990. Progress in Understanding Jointing over the Past Century, pp. 313–336. https://doi.org/10.1130/SPE253-p313.
Pollard, D.D., Segall, P., 1987. Theoretical displacements and stresses near fractures IN rock: with applications to faults, joints, veins, dikes, and solution surfaces. In: Fracture Mechanics of Rock. Elsevier, pp. 277–349. https://doi.org/10.1016/B978-0-12-066266-1.50013-2.
Price, N.J., 1966. Fault and Joint Development: in Brittle and Semi-brittle Rock. Elsevier.
Procter, A., Sanderson, D.J., 2018. Spatial and layer-controlled variability in fracture networks. J. Struct. Geol. 108, 52–65. https://doi.org/10.1016/j.jsg.2017.07.008.
Rämö, O.T., Haapala, I., 2005. Chapter 12 rapakivi granites. Dev. Precambrian Geol. 14, 533–562. https://doi.org/10.1016/S0166-2635(05)80013-1.
Rawnsley, K.D., Rives, T., Petti, J.-P., Hencher, S.R., Lumsden, A.C., 1992. Joint development in perturbed stress fields near faults. J. Struct. Geol. 14 (8–9), 939–951. https://doi.org/10.1016/0191-8141(92)90025-R.
Ripa, M., Stephens, M.B., 2020. Chapter 10 Magmatism (1.6–1.4 Ga) and Mesoproterozoic sedimentation related to intracratonic rifting coeval with distal accretionary orogenesis. Geol. Soc., Lond., Memoirs 50 (1), 269–288. https://doi.org/10.1144/M50-2017-4.
Rotevatn, A., Kristensen, T.B., Ksienzyk, A.K., Wemmer, K., Henstra, G.A., Midtkandal, I., Grundvåg, S.A., Andresen, A., 2018. Structural inheritance and rapid rift-length establishment in a multiphase rift: the East Greenland rift system and its caledonian orogenic ancestry. Tectonics 37 (6), 1858–1875. https://doi.org/10.1029/2018TC005018.
Samsu, A., Cruden, A.R., Micklethwaite, S., Grose, L., Vollgger, S.A., 2020. Scale matters: the influence of structural inheritance on fracture patterns. J. Struct. Geol. 130 (May 2019), 103896. https://doi.org/10.1016/j.jsg.2019.103896.
Sanders, C.A.E., Fullarton, L., Calvert, S., 2003. Modelling fracture systems in extensional crystalline basement. Geol. Soc., Lond., Spl. Publ. 214 (1), 221–236. https://doi.org/10.1144/GSL.SP.2003.214.01.13.
Sanderson, D.J., Nixon, C.W., 2015. The use of topology in fracture network characterization. J. Struct. Geol. 72, 55–66. https://doi.org/10.1016/j.jsg.2015.01.005.
Sanderson, D.J., Peacock, D.C.P., 2020. Making rose diagrams fit-for-purpose. Earth Sci. Rev. 201 (September 2019) https://doi.org/10.1016/j.earscirev.2019.103055.
Scheiber, T., Viola, G., 2018. Complex bedrock fracture patterns: a multipronged approach to resolve their evolution in space and time. Tectonics 37 (4), 1030–1062. https://doi.org/10.1002/2017TC004763.
Scholz, C.H., 2019. The mechanics of earthquakes and faulting. In: The Mechanics of Earthquakes and Faulting. https://doi.org/10.1017/9781316681473.
Segall, P., Pollard, D.D., 1980. Mechanics of discontinuous faults. J. Geophys. Res.: Solid Earth 85 (B8), 4337–4350. https://doi.org/10.1029/JB085iB08p04337.
Segall, P., Pollard, D.D., 1983. Nucleation and growth of strike slip faults in granite. J. Geophys. Res. 88 (B1), 555. https://doi.org/10.1029/JB088iB01p00555.
Skyttä, P., Torvela, T., 2018. Brittle reactivation of ductile precursor structures: the role of incomplete structural transposition at a nuclear waste disposal site, Olkiluoto, Finland. J. Struct. Geol. 116 (December 2017), 253–259. https://doi.org/10.1016/j.jsg.2018.06.009.
Stearns, D.W., 1969. Fracture as a mechanism of flow in naturally deformed layered rocks. In: Proceedings of the Conference on Research in *Tectonics, Kink Bands and Brittle Deformation*. Geological Survey of Canada, Papers, vol. 68, pp. 79–96, 52.
Torabi, A., Alaei, B., Ellingsen, T.S.S., 2018. Faults and fractures in basement rocks, their architecture, petrophysical and mechanical properties. J. Struct. Geol. 117 (June), 256–263. https://doi.org/10.1016/j.jsg.2018.07.001.
Vaasjoki, M., 1977. Rapakivi granites and other postorogenic rocks in Finland: their age and the lead isotopic composition of certain associated galena mineralizations. Geol. Surv. Finl. Bull. 11 (16), 1–71. https://inis.iaea.org/search/search.aspx?orig_q=RN:11543688.

Valkama, M., Sundblad, K., Nygård, R., Cook, N., 2016. Mineralogy and geochemistry of indium-bearing polymetallic veins in the Sarvlaxviken area, Lovisa, Finland. Ore Geol. Rev. 75, 206–219. https://doi.org/10.1016/j.oregeorev.2015.12.001.

Viola, G., Mattila, J., Zwingmann, H., Todd, A., Raven, M., 2011. Structural and K/Ar Illite Geochronological Constraints on the Brittle Deformation History of the Olkiluoto Region , Southwest Finland Structural and K/Ar Illite Geochronological Constraints on the Brittle Deformation History of the Olkiluoto Region.

Viola, G., Venvik Ganerød, G., Wahlgren, C.H., 2009. Unraveling 1.5 Ga of brittle deformation history in the Laxemar-Simpevarp area, southeast Sweden: a contribution to the Swedish site investigation study for the disposal of highly radioactive nuclear waste. Tectonics 28 (5), 1–29. https://doi.org/10.1029/2009TC002461.

Wan, X.G., Wu, G.H., Yang, P.F., Gao, L.H., 2016. The seismic technique description of carbonate fault damage zone in Halahatang area, Tarim basin. Oil Gas Geol. 37, 785–791.

Watkins, H., Healy, D., Bond, C.E., Butler, R.W.H., 2018. Implications of heterogeneous fracture distribution on reservoir quality; an analogue from the Torridon Group sandstone, Moine Thrust Belt, NW Scotland. J. Struct. Geol. 108, 180–197. https://doi.org/10.1016/j.jsg.2017.06.002.

Woodcock, N.H., Fischer, M., 1986. Strike-slip duplexes. J. Struct. Geol. 8 (7), 725–735. https://doi.org/10.1016/0191-8141(86)90021-0.

Wu, G., Gao, L., Zhang, Y., Ning, C., Xie, E., 2019. Fracture attributes in reservoir-scale carbonate fault damage zones and implications for damage zone width and growth in the deep subsurface. J. Struct. Geol. 118 (February 2017), 181–193. https://doi.org/10.1016/j.jsg.2018.10.008.

Yuguchi, T., Tagami, M., Tsuruta, T., Nishiyama, T., 2012. Three-dimensional fracture distribution in relation to local cooling in a granitic body: an example from the Toki granitic pluton, Central Japan. Eng. Geol. 149–150, 35–46. https://doi.org/10.1016/j.enggeo.2012.08.009.